Ore Geology Reviews 163 (2023) 105810

Contents lists available at ScienceDirect

Ore Geology Reviews

journal homepage: www.elsevier.com/locate/oregeorev

Controls on the metal tenors of sulfide ores in the Jinchuan Ni–Cu–PGE sulfide deposit, NW China: Implications for the formation of distinct textural types of sulfide ores in magma conduits

Yuhua Wang [a], Jianqing Lai [a], Yonghua Cao [a,*], Matthew Brzozowski [b], Xiancheng Mao [a], Hongwei Peng [c], Qixing Ai [d]

[a] Key Laboratory of Metallogenic Prediction of Nonferrous Metals and Geological Environment Monitoring (Ministry of Education), School of Geosciences and Info-Physics, Central South University, Changsha 410083, China
[b] British Columbia Geological Survey, 1810 Blanshard Street, Victoria, BC V8T 4J1, Canada
[c] State Key Laboratory of Ore Deposit Geochemistry, Institute of Geochemistry, Chinese Academy of Sciences, Guiyang 550081, China
[d] Nickel Cobalt Research and Design Institute, Jinchuan Group Co., Ltd., Jinchang 737104, China

ARTICLE INFO

Keywords:
Sulfide liquid fractionation
R factor
Metal tenor
Conduit-type deposit
Sulfide ore type
Jinchuan Ni–Cu–PGE deposit

ABSTRACT

The giant Jinchuan Ni–Cu–platinum-group element (PGE) sulfide deposit is a magma conduit system comprising four main intrusive units termed segments III, I, II-W, and II-E. The deposit comprises disseminated, net-textured, massive sulfide, and Cu-rich sulfide ores, with variations in metal tenors occurring among these different ore types and among the segments. Controls on these metal tenor variations must be linked to metallogenic processes, but this remains poorly constrained. To asses this, we systematically compared metal tenors (Ni, Cu, and the PGE) of ores from two perspectives — i) different ore types in each segment and ii) a single ore type across all four segments. Two major styles of metal tenor variations are documented. *Style 1*: Segments III and I have higher metal tenors than segments II-W and II-E for any given type of ore. Based on sulfide segregation models, this variation is interpreted to be related to variable degrees of early removal of sulfide liquid from the magmas that formed the four segments. *Style 2*: Disseminated ores in segments III and I have higher metal tenors than the other ore types, whereas all of the ore types in segments II-W and II-E have similar metal tenors. This is interpreted to be the result of the disseminated ores in segments III and I having formed from sulfide liquids that experienced higher R factors than the sulfide liquids that formed the other ore types, whereas all of the ores in segments II-W and II-E formed from sulfide liquids that experienced similar R factors. This difference suggests that the different ore types in segments III and I formed via early percolation and accumulation of sulfide liquids (the net-textured and massive ores) followed by the capture of disseminated, high R factor sulfides (the disseminated ore), whereas the different ore types in segments II-W and II-E likely formed by the physical percolation of originally disseminated sulfide liquid through the inter-crystal pore space. This study demonstrates that both sulfide ore texture and their metal-tenor variations are critical to characterizing ore-forming processes in dynamic magma conduits.

1. Introduction

The concept of an open-system magma conduit has been widely invoked to account for the disparity between the volume of magma represented by small mafic–ultramafic intrusions and the volume of the sulfides that they host (*e.g.*, Li and Ripley, 2009; Ding et al., 2012; Lightfoot et al., 2012). The formation of conduit-type, Ni–Cu–platinum-group element (PGE) sulfide deposits involves the transport, segregation, accumulation, and percolation of dense, immiscible sulfide liquid droplets (Robertson et al., 2016; Barnes et al., 2016, 2017; Yao et al., 2019). This complexity in processes is often accompanied by significant variability in metal tenors across different types of sulfide ores (*e.g.*, disseminated, net-textured, and massive sulfide) (Naldrett et al., 2009; Tonnelier, 2010; Lightfoot et al., 2012; Barnes et al., 2017). The variability in metal tenors results from the interplay of diverse magmatic and post-magmatic processes (Barnes et al., 2017), including

* Corresponding author.
E-mail address: yonghua@csu.edu.cn (Y. Cao).

https://doi.org/10.1016/j.oregeorev.2023.105810
Received 26 February 2023; Received in revised form 18 November 2023; Accepted 5 December 2023
Available online 9 December 2023

(1) crustal contamination of magmas (Ripley and Li, 2013; Samalens et al., 2017), (2) early segregation of sulfide liquids (Barnes and Ripley, 2016), (3) interaction between sulfide liquid and silicate magma (*i.e.,* R factor, Barnes and Lightfoot, 2005; Brzozowski et al., 2020; Brzozowski et al., 2021a; Brzozowski et al., 2021b), (4) sulfide liquid differentiation (Dare et al., 2014; Mansur et al., 2021), (5) early precipitation of platinum-group minerals (PGMs) from sulfide liquids or silicate magmas (Dare et al., 2014; Anenburg and Mavrogenes, 2016), and (6) hydrothermal alteration of magmatic sulfides (Holwell et al., 2017; Brzozowski et al., 2023). A comprehensive investigation into the roles and relative importance of these processes in controlling the variability of metal tenors of sulfide ores in conduit-type Ni–Cu–PGE sulfide deposits would help clarify the mechanisms of formation of different types of sulfide ores, and improve our understanding of ore-forming processes in these dynamic, flow-through magmatic systems (Ding et al., 2012; Robertson et al., 2016; Barnes et al., 2017; Barnes et al., 2018).

The Jinchuan Ni–Cu–PGE sulfide deposit, located on the southwestern margin of the North China Craton, is the third largest Ni–Cu–PGE sulfide deposit in the world, containing approximately 620 million tons (Mt) of sulfide ore at an average grade of 1.1 wt% Ni and 0.7 wt% Cu (Kang et al., 2022). The Jinchuan intrusion consists of four elongate, ultramafic segments; from west to east, these segments are termed segments III, I, II and IV. The deposit is widely considered to have formed by the segregation of sulfide liquid from a high-Mg, basaltic magma and subsequent enrichment of this sulfide liquid in metals by interaction with the magma in a dynamic conduit system (Chai and Naldrett, 1992a; Song et al., 2009, 2012; Tonnelier, 2010; Chen et al., 2013). It, therefore, serves as an excellent case study to investigate the mechanisms that control variations in metal tenors of sulfide ores in dynamic conduit systems.

Despite that the metal tenors of sulfide ores in several segments of the Jinchuan deposit have been previously characterized (*e.g.*, Chai and Naldrett, 1992b; Li and Ripley, 2011; Chen et al., 2013; Duan et al., 2016; Kang et al., 2022; Wang et al., 2022; Long et al., 2023), the key factors controlling the metal-tenor variations remain equivocal. A systematic comparison of metal tenors across all segments of the Jinchuan deposit may provide insights into the complex ore-forming processes that operated to form the deposit. Furthermore, the mechanisms that resulted in the formation of the different ore types in the Jinchuan deposit are not well constrained. For example, based on the morphology and particle size distribution of olivine grains and sulfides in segments I and II, Mao et al. (2018) proposed that the net-textured ores formed via a physical mechanism involving percolation of disseminated sulfide liquids through inter-olivine pore space in a mush zone. However, disseminated ores in Segment III have higher PGE tenors than the associated net-textured ores, which was ascribed by Kang et al. (2022) to be the result of upgrading of the sulfide liquid by interaction with PGE-undepleted magma. A detailed comparison of the metal tenors of the different types of sulfide ores from all segments of the Jinchuan deposit may provide further constraints on this topic.

In this contribution, whole-rock lithophile- and chalcophile-element concentrations of different ore types from segments III, I, and II are characterized, as well as the trace-element concentrations of pentlandite. Using this data, metal tenors (*e.g.*, Ni, Cu, and PGE) of the different ore types (disseminated, net-textured, massive, and Cu-rich ores) are calculated and compared in the context of i) different ore types in each segment and ii) a single ore type across different segments. Variations in metal tenors are discussed in terms of sulfide segregation, migration, accumulation, and post-magmatic alteration in a dynamic conduit system. The behavior of Cu, Se, and PGE in each segment during progressive enrichment is modeled using a multi-stage dissolution upgrading model, highlighting the kinetic mechanisms that generated the variations in metal tenor observed in each of the segments. Together, these findings offer valuable insights into the mechanisms of formation of the distinct ore types within different segments of the Jinchuan deposit. To our knowledge, this is the first study that has comprehensively compared the metal tenors of the different types of sulfide ores across all segments of the Jinchuan deposit, and related the metal tenor variations to contrasting ore-forming processes that operated in the different segments, providing valuable insights into the complexity of ore-forming processes of the Jinchuan deposit. Additionally, it is the first study that has quantified the importance of multiple magmatic pulses to metal enrichment in the different segments of the Jinchuan deposit, providing a direct means to examine the physicochemical dynamics of different portions of the conduit system.

2. Geologic background

The Jinchuan Ni–Cu–PGE sulfide deposit is located in the Longshoushan Terrane in the westernmost portion of the North China Craton (Fig. 1a). The Longshoushan Terrane is a long and narrow NE-trending belt comprising Neoproterozoic and Paleozoic sedimentary rocks (e.g., conglomerates, sandstones, and limestones) that are unconformably underlain by paleo-Mesoproterozoic metamorphic units (Fig. 1b; Tang and Li, 1995). The metamorphic basement units of the Longshoushan Terrane comprise the Baijiazuizi and Tamazigou formations (Fig. 1c). The Baijiazuizi Formation is the country rock to the Jinchuan deposit, and comprises mainly marble and migmatite. The Tamazigou Formation is dominated by schist, gneiss, and graphite-bearing marble (Song et al., 2006).

The NW–SE-trending Jinchuan intrusion is ~ 6500 m long and 20–527 m wide, with an exposed area of ~ 1.4 km^2. The intrusion dips to the southwest at angles of 50–80°, and was emplaced into paleo-Mesoproterozoic metamorphic gneiss, schist, marble, and granite (Fig. 2a; Tang and Li, 1995). The emplacement age of the Jinchuan intrusion has been constrained to 831.8 ± 0.6 Ma based on zircon and baddeleyite U–Pb geochronology (Zhang et al., 2010). A series of NE-trending strike–slip faults, namely the F_8, F_{16-1}, and F_{23}, divide the Jinchuan intrusion into four segments, which, from west to east, are segments III, I, II, and IV (Fig. 2b-g). Segment II has been displaced by the F_{17} Fault and has been further subdivided into Segment II-W in the west and Segment II-E in the east (Fig. 2a, Duan et al., 2016; Mao et al., 2018; Mao et al., 2019). Previous studies proposed that the segments on either side of the F_{16-1} Fault represent two separate intrusions (*i.e.,* the Eastern and Western intrusions, Song et al., 2009, 2012; Chen et al., 2013; Duan et al., 2016). However, a recent study by Kang et al. (2022) demonstrated that sulfide ores in Segment III have textures and PGE grades that are distinct to those of Segment I, and suggested that these segments represent independent intrusions despite their location on the western side of the F_{16-1} Fault (Kang et al., 2022). Given the significant mining activity in, and data availability for, segments III, I, II-W, and II-E, they are the focus of this study. Segment IV is still under initial exploration and data availability is limited.

2.1. Segment III

Segment III is located west of the F_8 Fault (Fig. 2a). The Jinchuan intrusion in this segment strikes 10–30° NW. The main lithologies are dunite, lherzolite, and plagioclase-bearing lherzolite. These rocks were locally crosscut by a network of 0.5–10 mm-wide carbonate and/or quartz veins (Fig. 3a). Based on the grain size of olivine and the sharp contact between different lithologies, Segment III was subdivided into upper and lower cycles. From bottom to top, the upper cycle mainly comprises fine-grained (0.5–3 mm) dunite, lherzolite, and pyroxenite (Chen et al., 2013). The lower cycle is also composed mainly of dunite, lherzolite, and pyroxenite, but the grain size is coarser (6–10 mm) (Kang et al., 2022). Based on the presence of fine-grained dunite xenoliths at the top of the lower cycle, the lower cycle is considered to have been emplaced slightly later than the upper cycle (Song et al., 2012). Rock units in Segment III were extensively altered, with olivine and pyroxene largely replaced by serpentine and chlorite + tremolite, respectively. This segment hosts the recently identified No. 3 orebody (Kang et al.,

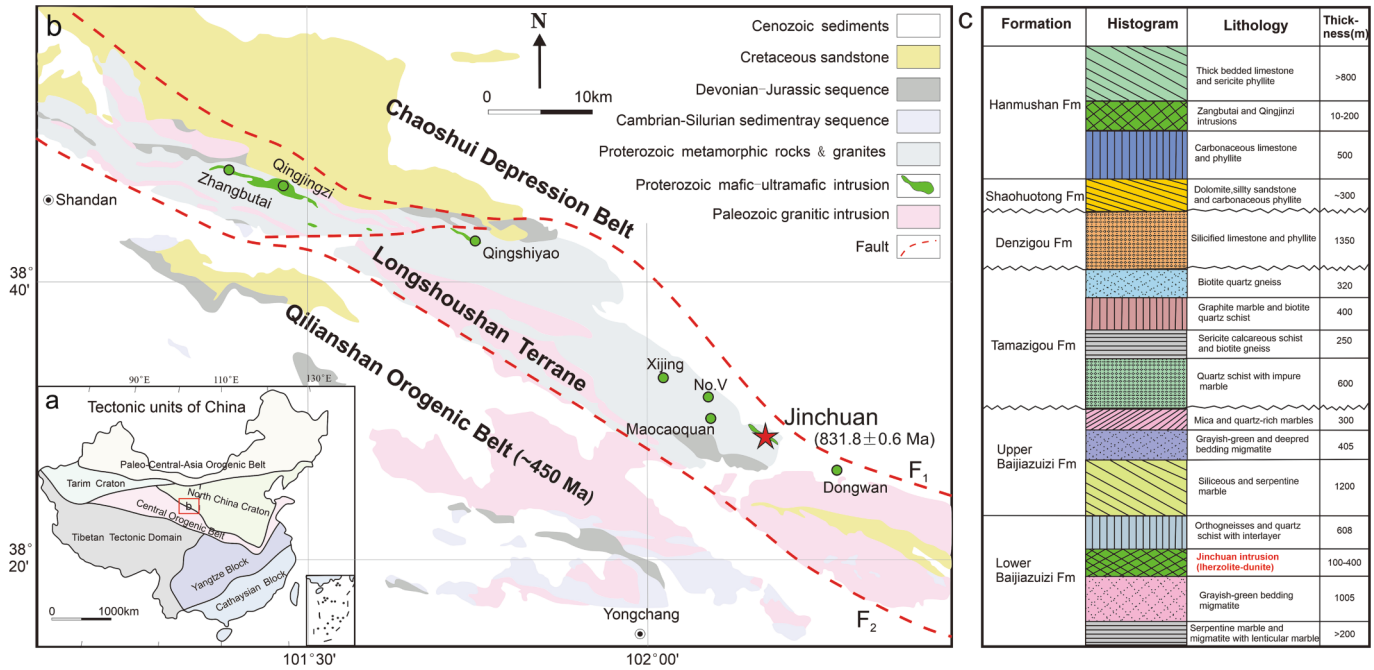

Fig. 1. (a) Simplified geologic map illustrating the main tectonic units of China. (b) Simplified regional geologic map illustrating the location of the Jinchuan deposit and several other mafic–ultramafic intrusions in the Longshoushan Terrane (modified after Song et al., 2009). (c) Stratigraphic summary of the Longshoushan Terrane (modified after Tang and Li, 1995).

2022), in which disseminated and net-textured sulfide mineralization are common, but massive sulfide mineralization is rare (Fig. 2c). Layers of disseminated ore are 30–150 m thick and occur at depths of 1100–1600 m, whereas layers of net-textured ore are ~ 60 m thick and occur at depths of 1100–1400 m. The layers of both types of ore thicken towards the east, suggesting that the orebodies may extend into Segment I (Chen et al., 2013; Kang et al., 2022).

2.2. Segment I

Segment I occurs between the F_8 and F_{16-1} faults. The exposed intrusion has a length of 1500 m along a strike of 44° NW (Fig. 2d) and appears to narrow from west to east. Similar to Segment III, rock units in this segment were divided into upper and lower cycles based on the grain size of olivine (Chen et al., 2013). The upper cycle consists of fine-grained dunite and is weakly mineralized, with minor sulfides occurring interstitial to olivine and pyroxene (Song et al., 2012). The lower cycle is composed of coarse-grained lherzolite and hosts a significant amount of sulfides (*i.e.,* some of the rocks represent an olivine–sulfide cumulate). The sulfide-bearing olivine cumulate is overlain by sulfide-poor, coarse-grained lherzolite; minor pyroxenite occurs at the base of the lower cycle (Chen et al., 2013). The rocks comprising this segment were also highly altered. Segment I is dominated by the No. 24 orebody, which contains three textural types of sulfide ores — disseminated, net-textured, and Cu-rich ores. The thickness of the disseminated ores generally increases towards the western portion of this segment, whereas the net-textured ores are typically concentrated near the bottom of the intrusion and intrude the marble country rocks (Fig. 3b, c). Recently, a lenticular, Cu-rich orebody was discovered at depths of 1070–1140 m and to the right of the No. 24 orebody in this segment, the shape of which is thought to have been controlled by regional tectonics (Jiao et al., 2012). The Cu-rich orebody locally contains sulfide-poor, ultramafic breccias, with diameters of 0.1–5 cm, reflecting the injection of Cu-rich sulfide liquids into the pre-existing, barren ultramafic rock (Fig. 3d). Locally, the Cu-rich sulfide mineralization intrudes along fractures in the country rock marble (Fig. 3e).

2.3. Segments II-W and II-E

The Jinchuan intrusion on the east side of the F_{16-1} Fault was divided into segments II and IV by the F_{23} Fault (Fig. 2a). Again, Segment II consists of upper and lower cycles. The upper cycle has a plate-like morphology, extends to depths of 300–400 m, and contains disseminated sulfides hosted by coarse-grained lherzolite (Song et al., 2012; Chen et al., 2013). The lower cycle is approximately four times larger than the upper cycle and extends to depths of 200 m to > 1100 m (Tang and Li, 1995). This cycle is economically significant because it contains two large, net-textured sulfide orebodies. Locally, sulfide-poor and massive sulfide ores also occur in the lower cycle. The intrusion in Segment II, which strikes 50° NW, was further divided into II-W and II-E roughly along exploration line 28 based on a zone of the intrusion lacking mineralization (Fig. 2b). Segments II-W and II-E contain the two largest orebodies in the Jinchuan deposit (*i.e.,* the No. 1 and 2 orebodies).

The No. 1 orebody in Segment II-W is ~ 1600 m long, has an average thickness of ~ 90 m, and extends to a depth of 200 m to > 1000 m. It contains ~ 50 % of the total Ni Cu, and PGE reserves of the Jinchuan deposit (Song et al., 2012). The overall distribution of sulfide ores and host rocks in this segment are nearly concentrical, with massive and net-textured ores occurring in the center, and disseminated ores occuring along the peripheries of the segment, the latter of which grades outwards into barren lherzolite (Fig. 2e). The No. 2 orebody in Segment II-E occurs at a comparatively shallow depth of 600–850 m, with a length of ~ 1300 m and an average thickness of ~ 120 m (Fig. 2b). Sufides accumulated at the bottom of the No. 2 orebody to form a net-textured and massive sulfide lens that dips to the SW (Fig. 2b). In plan view, the No. 2 orebody is concentrically zoned, with a central zone dominated by massive and net-textured ores, and the periphery dominated by disseminated ores, similar to the No. 1 orebody (Fig. 2g) (Tang and Li, 1995). The massive ores have sharp boundaries with their host rocks, and contain inclusions of ultramafic and metamorphic rocks (Fig. 3f) (Song et al., 2009).

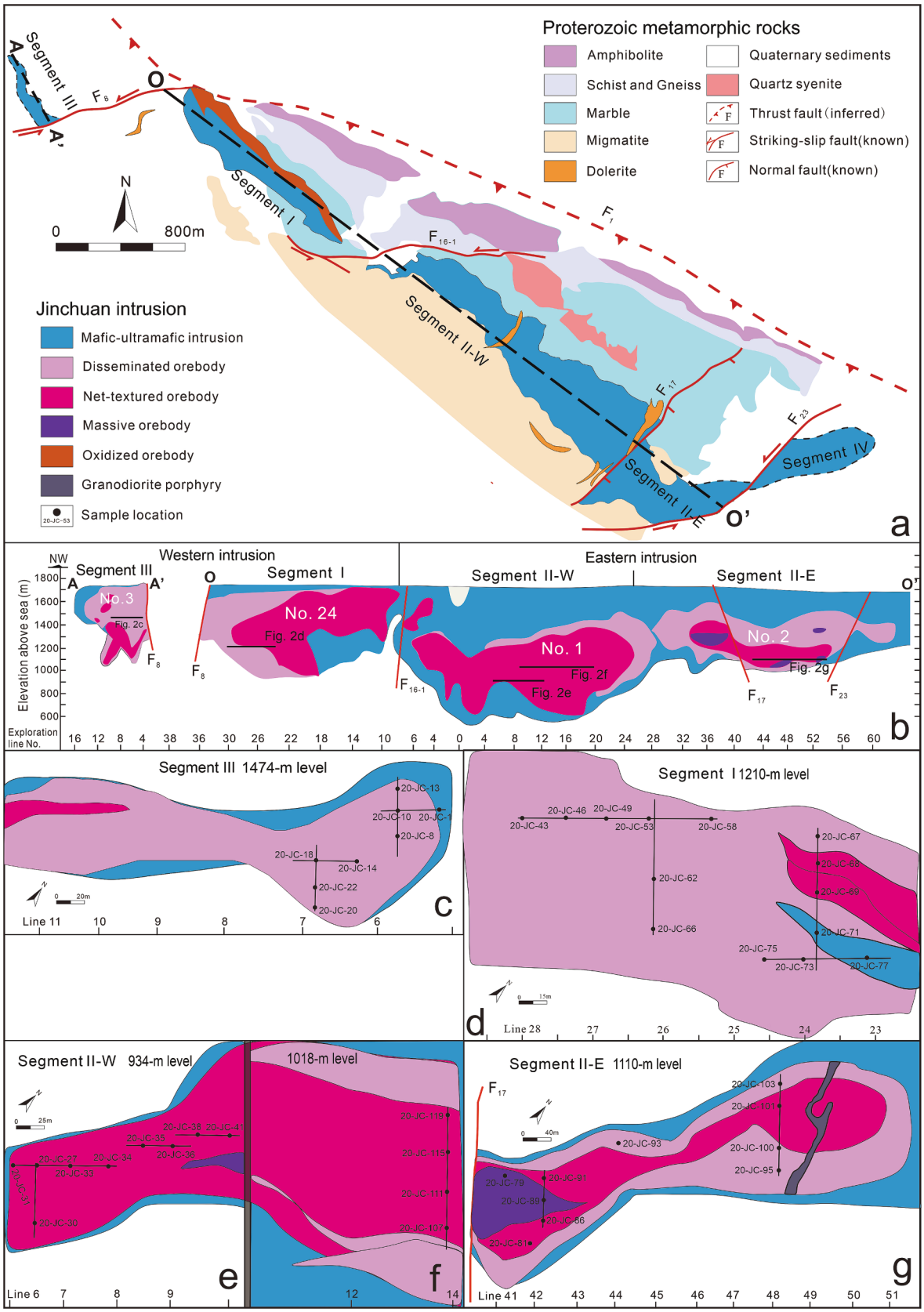

Fig. 2. (a) Distribution of segments, mafic–ultramafic intrusions, and faults in the Jinchuan deposit (modified after Duan et al., 2016). (b) A projected long section showing the Western and Eastern intrusions, segments of the Jinchuan deposit, and the location of mineralization. (c, d, e, f, g) Plan views of selected segments highlighting the locations of samples.

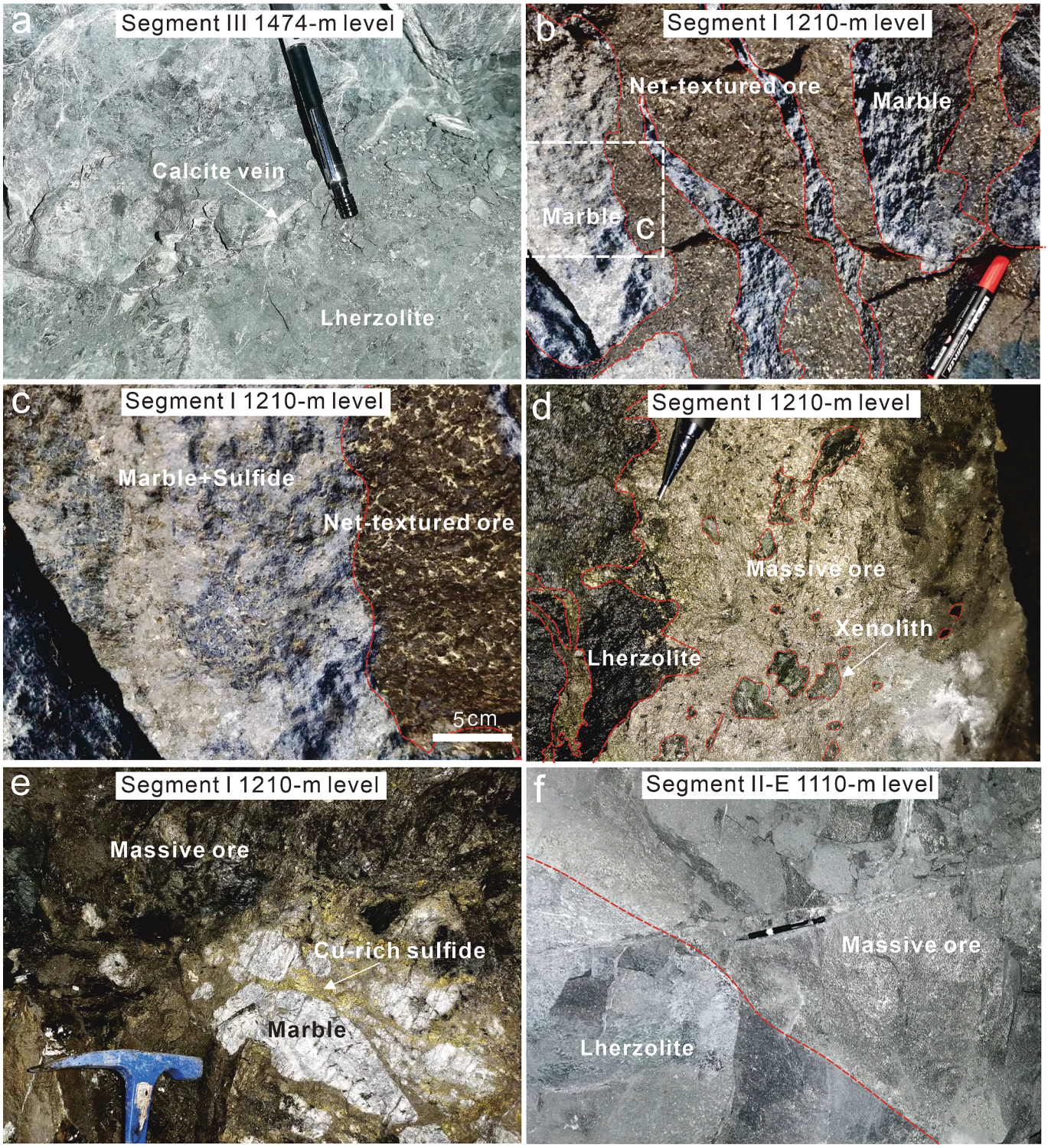

Fig. 3. Underground photographs of ultramafic rocks and ores. (a) Segment III: calcite veins that crosscut lherzolite. (b, c) Segment I: irregular contact between net-textured ore and the marble country rocks. Mafic minerals and sulfides are observed in the marble. (d) Segment I: irregular contact between a massive sulfide orebody and lherzolite. Note the ultramafic xenoliths within the orebody. (e) Segment I: stockwork Cu-rich sulfides along fractures in the marble country rocks. (f) Segment II-E: sharp boundary between massive ore and barren lherzolite.

3. Descriptions of sulfide ores

Sulfides in disseminated ores from the Jinchuan deposit occur as irregularly shaped, polymineralic blebs interstitial to silicate minerals and as micro-inclusions in silicate minerals (Fig. 4a, ESM Fig. 1a, b). Sulfides are mainly composed of pyrrhotite (50–70 modal%), chalcopyrite (5–15 modal%), and pentlandite (5–10 modal%), with minor cubanite (<3 modal%) and pyrite (<2 modal%) (Fig. 4a-c). Pyrrhotite mainly occurs as discrete grains interstitial to silicate minerals (Fig. 4b). Pentlandite mainly occurs as grains that are enclosed within pyrrhotite (Fig. 4b, c), but also occur locally as exsolution flames within pyrrhotite. Chalcopyrite commonly occurs on the edges of, or as grains

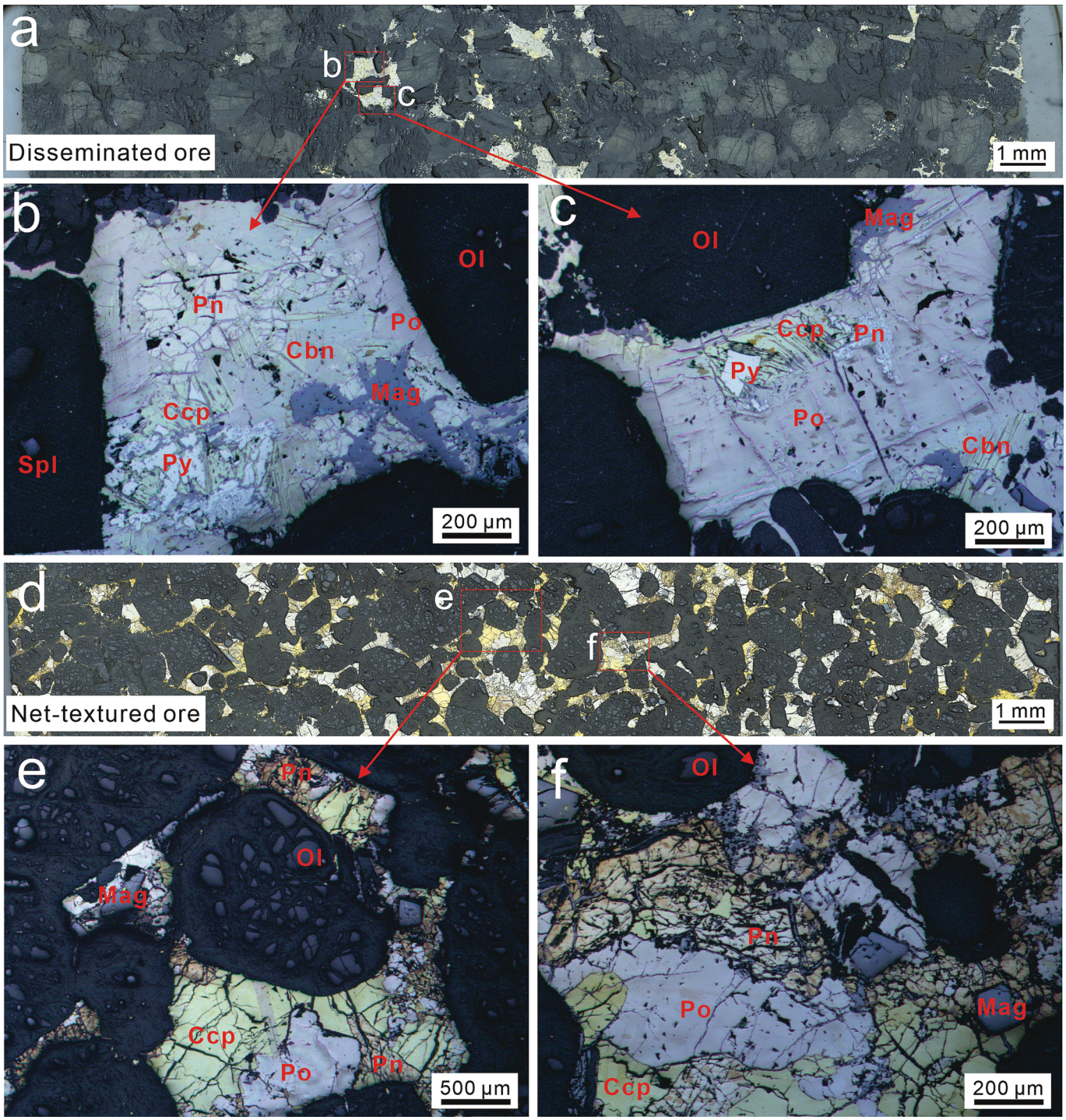

Fig. 4. Scans and reflected-light photomicrographs of disseminated and net-textured ores from segments II-W and II-E. (a–c) disseminated ore and (d–f) net-textured ores. Abbreviations: Cbn = cubanite, Ccp = chalcopyrite, Ol = olivine, Pn = pentlandite, Po = pyrrhotite, Py = pyrite, Spl = spinel, Mag = magnetite.

within, pyrrhotite and pentlandite (Fig. 4b, c). Cubanite occurs as laths in chalcopyrite (Fig. 4b, c). Fine-grained, cubic pyrite can occur within chalcopyrite (Fig. 4c). Most of the disseminated sulfides also contain irregularly shaped magnetite grains that are suggested to be hydrothermal in origin (Wang et al., 2023).

Sulfides in net-textured ores occur as irregular, interconnected networks of sulfide interstitial to silicate minerals and surrounding rounded olivine grains (ESM Fig. 1c, d). The sulfides mainly consist of pyrrhotite (20–60 modal%), pentlandite, and chalcopyrite (their abundances are highly variable, but are generally < 20 modal%), with minor cubanite (<5 modal%) and pyrite (<3 modal%) (Fig. 4d). The three volumetrically dominant sulfides (pyrrhotite, chalcopyrite, and pentlandite) commonly occur as composite sulfide aggregates (Fig. 4e, f). Irregularly shaped and nearly cubic magnetite grains are common within these sulfide aggregates (Fig. 4e, f).

Sulfides in the massive ores consist mainly of pyrrhotite (50–70 modal%), pentlandite (10–20 modal%), and chalcopyrite (<10 modal %), with minor cubanite (<5 modal%) and pyrite (<3 modal%) (Fig. 5a, ESM Fig. 1e, f). X-ray fluorescence maps of Ni–Cu–S highlight two types of pentlandite in the massive sulfide ores — coarse-grained, granular

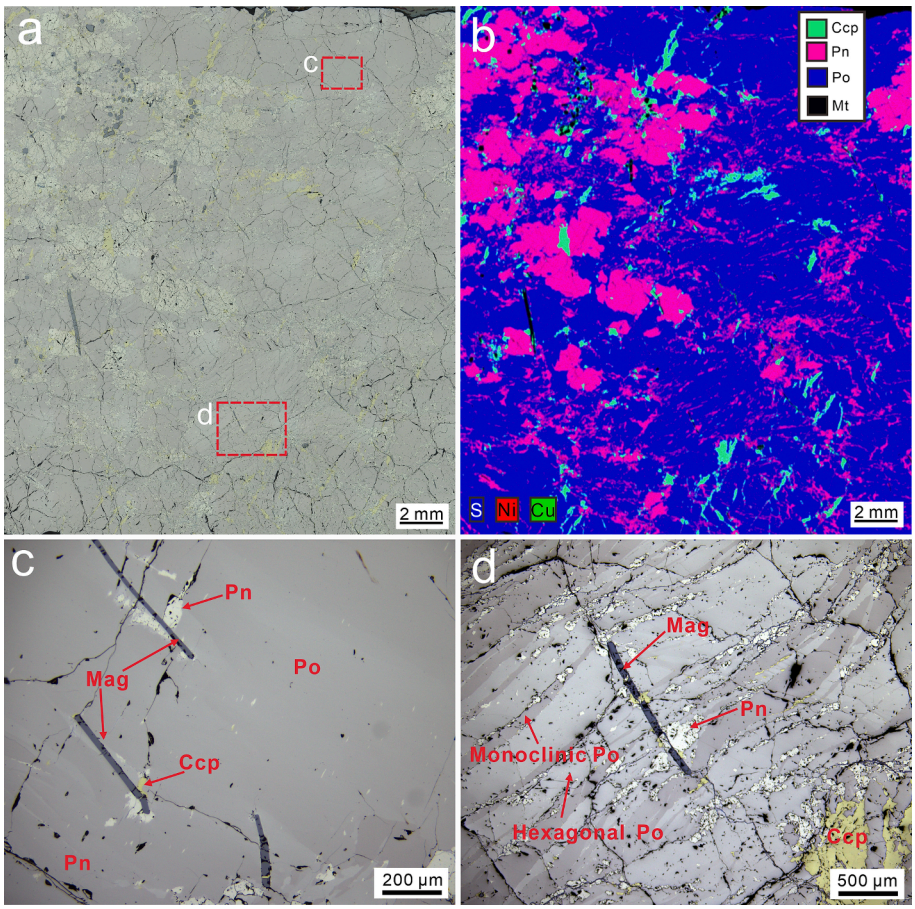

Fig. 5. (a) Scan and (b) S–Ni–Cu X-ray fluorescence map of a massive sulfide ore sample from Segment II-E. (c, d) Photomicrographs of portions of the same massive sulfide ore sample. Note the hexagonal and monoclinic pyrrhotite intergrowth in Fig. 5d.

pentlandite, and chain-like pentlandite aggregates that are commonly referred to as loop texture (Fig. 5b), the latter of which resulted from a peritectic reaction between early formed monosulfide solution (MSS) and residual Cu-rich sulfide liquids (Barnes et al., 2020). Pyrrhotite occurs as relatively large crystals enclosing smaller pentlandite and chalcopyrite grains (Fig. 5a, b). In addition to the blade-like, hexagonal crystals of pyrrhotite, it can also occur as intergrowths of hexagonal and monoclinic varieties (Fig. 5c, d). That is, monoclinic pyrrhotite can occur as parallel, blade-like exsolutions in a matrix of hexagonal pyrrhotite; this was also observed by Jiao et al. (2018) in massive sulfide ores of the Jinchuan deposit. Chalcopyrite (and cubanite) typically occur along the contact between pyrrhotite and pentlandite (Fig. 5c, d). Elongated assemblages of magnetite can also occur in the massive ores (Fig. 5a–d).

4. Sampling and analytical methods

4.1. Sampling

Forty-eight ore samples were collected from underground exposures of segments III, I, II-W, and II-E; their locations are indicated in Fig. 2c–f. Ten samples were collected from the 1474-m sub-level of Segment III, fifteen samples from the 1210-m sub-level of Segment I, thirteen samples from the 934-m and 1018-m sub-levels of Segment II-W, and ten samples from the 1100-m sub-level of Segment II-E. Sulfide abundances were calculated from whole-rock S contents and assuming a S content of 35.7 wt% for a typical pyrrhotite–pentlandite–chalcopyrite mixture (Kerr, 2001). The samples were then classified as disseminated (0.8–15 wt% sulfide), net-textured (15–65 wt% sulfide), and massive (>65 wt% sulfide) ore types following the classification of Barnes et al. (2017) (ESM Fig. 2). Based on this classification strategy, the majority of samples from segments III and I represent disseminated ore, with only one sample from Segment I representing massive ore. In contrast, samples from segments II-W and II-E largely represent net-textured ore, with few samples representing disseminated and massive ores. It should be emphasized that the term massive ore in this study refers to the regular massive ores without Cu enrichment (modal% of chalcopyrite < 50). Copper-rich massive ore containing > 50 modal% chalcopyrite is here termed Cu-rich ore.

4.2. Analytical methods

(1) Whole-rock PGE and chalcophile elements

The concentrations of S, Se, Ni, Cu, and PGE (Ir, Ru, Rh, Pd, Pt, except Os) were determined at the Test Center of Nonferrous Metals Geology and Mining Co. Ltd., Guilin, China. For the disseminated, net-textured, and massive ores, 10 g, 5–8 g, and 2–5 g powders, respectively, were used for analyses. The powdered samples were mixed with a flux of lithium metaborate and lithium tetraborate, and fused in an induction furnace. For whole-rock S, Se, Ni, and Cu analyses, the prepared samples were dissolved in aqua regia at 90°C for 2 h. Sulfur concentrations were determined via LECO (instrument model: SRJK-2.5-13WS). Nickel, Cu, and Se concentrations were determined by atomic absorption spectrometry (AAS, instrument model: Z-2010). For whole-rock PGE analyses, the prepared samples were mixed with alkaline fluxes, Ni and S in a ceramic crucible and shaken well, followed by fusion in a muffle furnace. After cooling, the NiS bead was separated

from the slag and dissolved in HCl using closed-cap PTFE-lined cups. The PGE were then co-precipitated with a Te-bearing HCl solution. Sample precipitates were then filtered and dissolved in aqua regia, and diluted for whole-rock PGE analysis by Ni sulfide fire assay with ICP–MS finish (instrument model: Thermo iCAP Q ICP–MS). Details of the analytical procedures and QA/QC controls are provided in Qi et al. (2004). Precision and accuracy were obtained by analyzing reference materials UMT-1 and WPR-1, which, for S, Se, Ni, and Cu, are both better than 8 %, and for PGE are both better than 10 %. Sulfur, Se, Ni, Cu, and PGE concentrations are provided in ESM Table S1.

(2) XRF element mapping

Micro X-ray fluorescence (uXRF) element mapping was completed in the Tuoyan Testing Technology Co., Ltd, Guangzhou, China using a Bruker M4 Plus uXRF analyzer. This instrument uses a multi-channel capillary X-ray beam, with a 20 μm spot size as the excitation source, an accelerating voltage of 50 kV, and a current of 300 μA. The instrument is equipped with two XFlash silicon drift detectors and is operated at a pressure of 3 mbar. The scanning step size for the maps was set to 10 μm and the dwell time per point analysis was set to 5 ms. The collected data were processed using the M4 Tornado software, which interprets spectral peak information and reports elemental distribution.

(3) Laser ablation ICP–MS analyses of pentlandite

The concentrations of PGE and chalcophile elements in pentlandite were determined by laser ablation inductively coupled plasma mass spectrometry (LA–ICP–MS) at the State Key Laboratory of Ore Deposit Geochemistry, Institute of Geochemistry, Chinese Academy of Sciences (IGCAS) using an Agilent 7700 × ICP–MS instrument coupled to a 193 nm RESOlution-LR-S155 excimer laser ablation system. Ablation was performed in a He atmosphere flowing at 0.35 L/min. The ablated aerosol was mixed with Ar (0.9 L/min) as a transport gas. The laser was operated at a spot size of 26 μm, a pulse rate of 5 Hz, and a fluence of 2.5–3 J/cm^2. The instrument was optimized using SRM610 to achieve the best sensitivity and ionization efficiency (U/Th ≈ 1), the lowest production of oxides (ThO/Th < 0.3 %), and low background values. The following analytes were determined: ^{34}S, ^{57}Fe, ^{59}Co, ^{60}Ni, ^{65}Cu, ^{66}Zn, ^{75}As, ^{77}Se, ^{99}Ru, ^{101}Ru, ^{102}Ru, ^{103}Rh, ^{105}Pd, ^{106}Pd, ^{108}Pd, ^{109}Ag, ^{111}Cd, ^{121}Sb, ^{125}Te, ^{185}Re, ^{189}Os, ^{193}Ir, ^{195}Pt, ^{197}Au, ^{208}Pb, and ^{209}Bi. The total acquisition time for each analysis was 90 s, and included 30 s of background acquisition (gas blank), and 60 s of ablation and signal acquisition. Concentrations were calculated using multiple external standards and the total normalization method (Liu et al., 2008). Standards STDGL3, Po725, and GSD-1G were used for external calibration of PGE and chalcophile elements. STDGL3, Po725, and MASS-1 were analyzed every 30–60 min when determining the concentrations of Re and PGE. An in-house pyrite standard was used for calibration of S concentrations. Sulfide reference material MASS-1 was used as an unknown sample to monitor the results. The detection limits of Pd, Pt, Ir, Os, Rh, and Ru in pentlandite are 0.0087 ppm, 0.0209 ppm, 0.0042 ppm, 0.0195 ppm, 0.0022 ppm, and 0.0022 ppm, respectively. The detection limits of other elements in pentlandite, along with the reference values of chalcophile elements in the sulfide standards, are provided in ESM Table S2.

5. Results

5.1. Inter-relationships between whole-rock Cu–Ni–Co–S–PGE contents of different sulfide ore types

Whole-rock Cu, Ni, Co, S, and PGE concentrations of the different types of sulfide ores from segments III, I, II-W, and II-E are provided in ESM Table S1; the average values are summarized in Table 1. Whole-rock Cu vs. S is plotted in Fig. 6a and includes control lines for chalcopyrite, pyrrhotite, and bornite constructed based on their ideal stoichiometric formulas. This plot has been demonstrated to be useful in highlighting differences in proportions of chalcopyrite and pyrrhotite in sulfide ores (*e.g.*, Cao et al., 2021). Disseminated, net-textured, and massive ores from the four segments plot largely between the 50:50 pyrrhotite:chalcopyrite and 95:5 pyrrhotite:chalcopyrite control lines (Fig. 6a), consistent with petrographic observation that sulfides in these ores contain < 50 modal% chalcopyrite. Copper-rich ores, however, plot closer to the chalcopyrite control line than most of the net-textured and massive ores, as expected given their greater abundance of chalcopyrite (Fig. 6a). When all of the ore types are considered together, Cu, Ni, Co, and the PGE are positively correlated with S, highlighting the chalcophile behavior of these elements (*i.e.*, they are principally hosted by sulfides; Fig. 6a–f). Individually, however, disseminated ores are characterized by positive correlations between Cu–Ni–Co–PGE and S, whereas the net-textured and massive ores are not (Fig. 6a–f).

Table 1
Summary of the average concentrations of Cu, Ni, and PGE, and their calculated tenors in different types of sulfide ores from different segments of the Jinchuan deposit.

Segment	Ore type	n	Ni	Cu	Ir	Ru	Rh	Pt	Pd	S	Ni tenor	Cu tenor	Ir tenor	Ru tenor	Rh tenor	Pt tenor	Pd tenor
			wt.%	wt.%	ppb	ppb	ppb	ppb	ppb	wt.%	wt.%	wt.%	ppb	ppb	ppb	ppb	ppb
Segment III	Diss	75	0.64	0.43	17.4	15.1	18.0	279.3	130.6	2.07	9.91	7.41	318.1	356.5	180.0	5194.6	2548.1
Segment III	Net	38	2.03	1.35	39.6	67.7	28.6	646.1	315.5	8.43	8.68	6.43	188.0	306.0	129.2	3213.0	1632.7
Segment I	Diss	87	0.59	0.41	13.1	17.1	7.11	240	125	1.99	9.94	7.41	308	355	163	5431	2846
Segment I	Net	50	2.45	1.97	38.7	39.9	17.2	1027	377	9.28	9.88	8.04	164	169	73.2	4048	1605
Segment I	Ms	20	5.11	2.40	373	489	157	51.4	482	31.30	6.31	3.16	461	628	193	70.2	593
Segment I	Cu-rich	17	2.21	2.84	1.53	2.08	2.45	910	613	8.47	9.10	12.25	6.68	10.8	10.6	3874	2727
Segment II-W	Diss	66	0.79	0.48	9.84	11.8	7.50	170	99.3	2.68	9.58	6.14	125	154	110	1783	1215
Segment II-W	Net	135	1.96	1.59	27.8	32.21	22.2	679	291	8.25	8.56	7.19	134	155	65.3	1068	1183
Segment II-E	Diss	64	0.61	0.38	3.09	3.84	4.97	36.1	25.0	2.47	7.76	5.53	43.2	65.1	90.2	557	510
Segment II-E	Net	52	1.88	1.17	12.0	19.6	10.7	56.6	82.2	9.32	7.23	4.96	52.7	87.9	40.6	228	330
Segment II-E	Ms	22	6.52	2.57	29.8	47.8	21.8	34.7	128	29.05	8.51	3.18	36.5	61.6	27.3	41.5	169

Abbreviations: Diss = disseminated, Net = net-textured, Ms = massive.

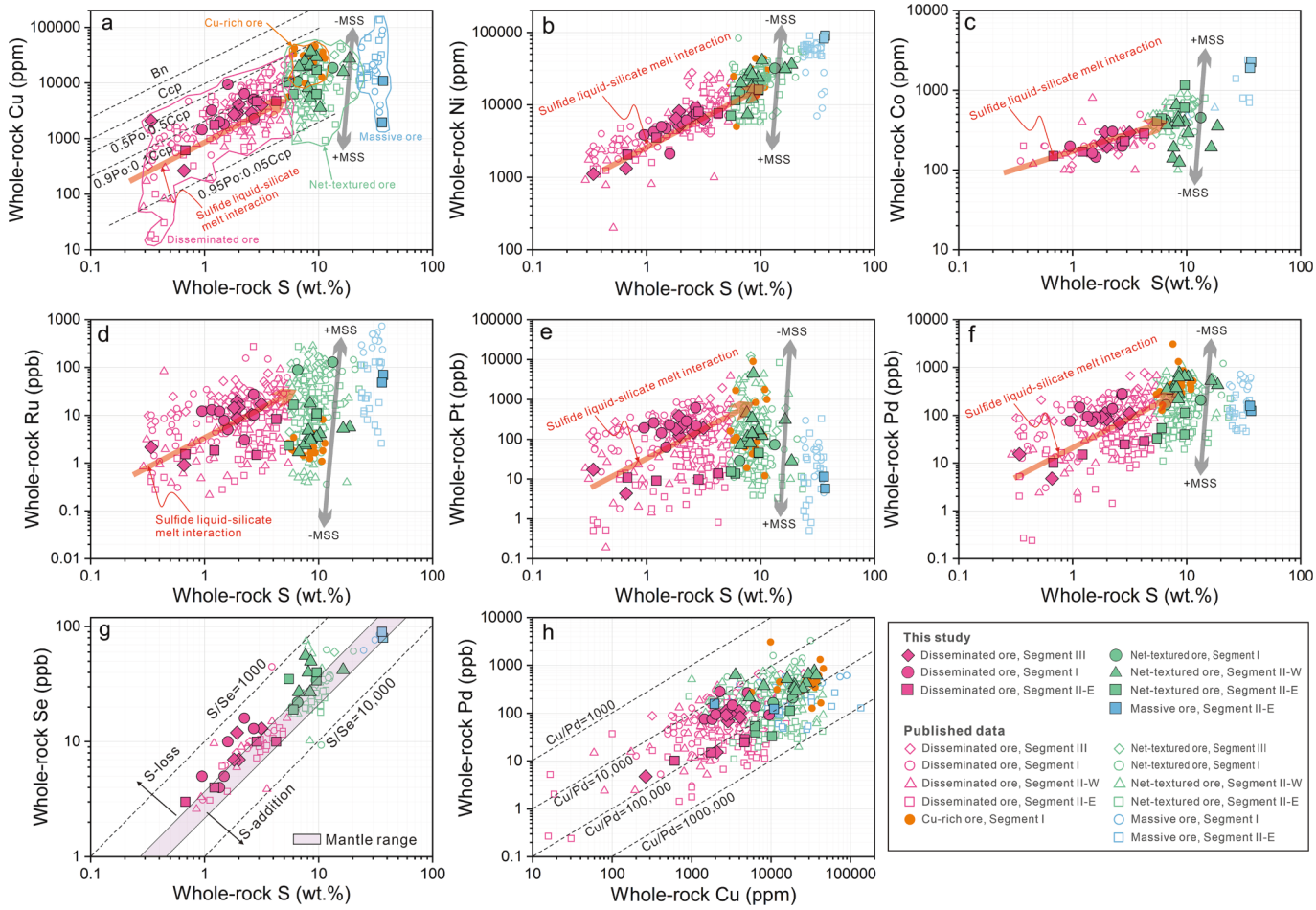

Fig. 6. Binary diagrams illustrating the variation between whole-rock S and (a) Cu, (b) Ni, (c) Co, (d) Ru, (e) Pt, (f) Pd, and (g) Se, and (h) between Cu and Pd for disseminated, net-textured, massive, and Cu-rich ores in the Jinchuan deposit. Sulfide control lines in (a) are constructed based on the stoichiometry of different sulfide minerals (e.g., pyrrhotite: $Fe_{0.9}S$, Cu/S = 0; chalcopyrite: $CuFeS_2$, Cu/S = 1; bornite: Cu_5FeS_4, Cu/S = 2.5). The mantle range for S/Se is from Eckstrand and Hulbert (1987). Data sources: this study, Chai and Naldrett (1992b), Su et al. (2008), Song et al. (2006), Song et al. (2009), Tonnelier (2010), Chen et al. (2013), Jiang et al (2014), Duan et al. (2016), Mao et al. (2019), Han (2021), and Kang et al. (2022).

5.2. Whole-rock S/Se and Cu/Pd

Sulfur and Se behave similarly during magmatic processes, but can fractionate during hydrothermal processes; whole-rock S/Se ratios can, therefore, be used to track magmatic–hydrothermal processes in Ni–Cu–PGE sulfide deposits (Queffurus and Barnes, 2015; Smith et al., 2016; Brzozowski et al., 2020). In the Jinchuan deposit, the sulfide ores largely exhibit good correlations between S and Se, with most samples having S/Se ratios within the range of mantle values (2632–4350; Eckstrand and Hulbert, 1987; Palme and O'Neill, 2014) (Fig. 6g). Some of the disseminated ore samples from segments I and III, and net-textured ore samples from segments II-W and II-E, however, have S/Se ratios that are lower than the mantle range (Fig. 6g). In addition, a few samples of disseminated and net-textured ores from segments I and II-W have S/Se ratios in the range of 10,000, which is notably higher than mantle values (Fig. 6g). The majority of samples from segments III, I, II-W, and II-E have Cu/Pd ratios that are higher than mantle values (1,000–10,000; Barnes et al., 2015) (Fig. 6h).

5.3. Cu, Ni, and PGE tenors

The different ore types from segments III, I, II-W, and II-E have different sulfide abundances. A robust comparison of their metal contents, therefore, requires recalculation of metal concentrations to 100 % sulfide (*i.e.,* their metal tenors). Metal tenors were calculated using equation (1) considering that metal tenors calculated by this equation have been demonstrated to match well the composition of sulfide separates (Barnes and Lightfoot, 2005):

$$C_i^{100} = 100C_i^{wr}/(2.527*S + 0.3408*Cu + 0.4715*Ni) \quad (1)$$

where C_i^{100} is the concentration of an element in 100 % sulfides, C_i^{wr} is the concentration of the element in the whole rock, and S, Cu, and Ni are whole-rock concentrations of these elements (in wt. %).

As Ni is partially hosted in silicates, mostly olivine, before calculating the Ni tenor, Ni hosted in silicates needs to be determined and subtracted. We followed the method of Song et al. (2009) to calculate the amount of Ni hosted by silicates in different types of sulfide ores. First, the relationship between whole-rock MgO and whole-rock Ni in S-poor samples (S < 0.1 wt%) was used to develop a regression equation — Ni^{wr} (wt. %) = 0.0037 * MgO^{wr} (wt. %) − 0.0049 (R^2 = 0.9). Second, given availability of the whole-rock MgO contents, this regression equation was applied to different types of sulfide ores to calculate the amount of Ni hosted by their silicates.

The calculated Cu, Ni, and PGE (IPGE + PPGE) tenors of the different ore types in each segment are illustrated in Fig. 7 and summarized in Table 1; the complete dataset is provided in ESM Table S3. Disseminated and net-textured ores in the four segments have indistinguishable Cu and Ni tenors that are generally higher than those in the massive ores in segments I and II-E (Fig. 7a, b). As expected, Cu-rich ores in Segment I

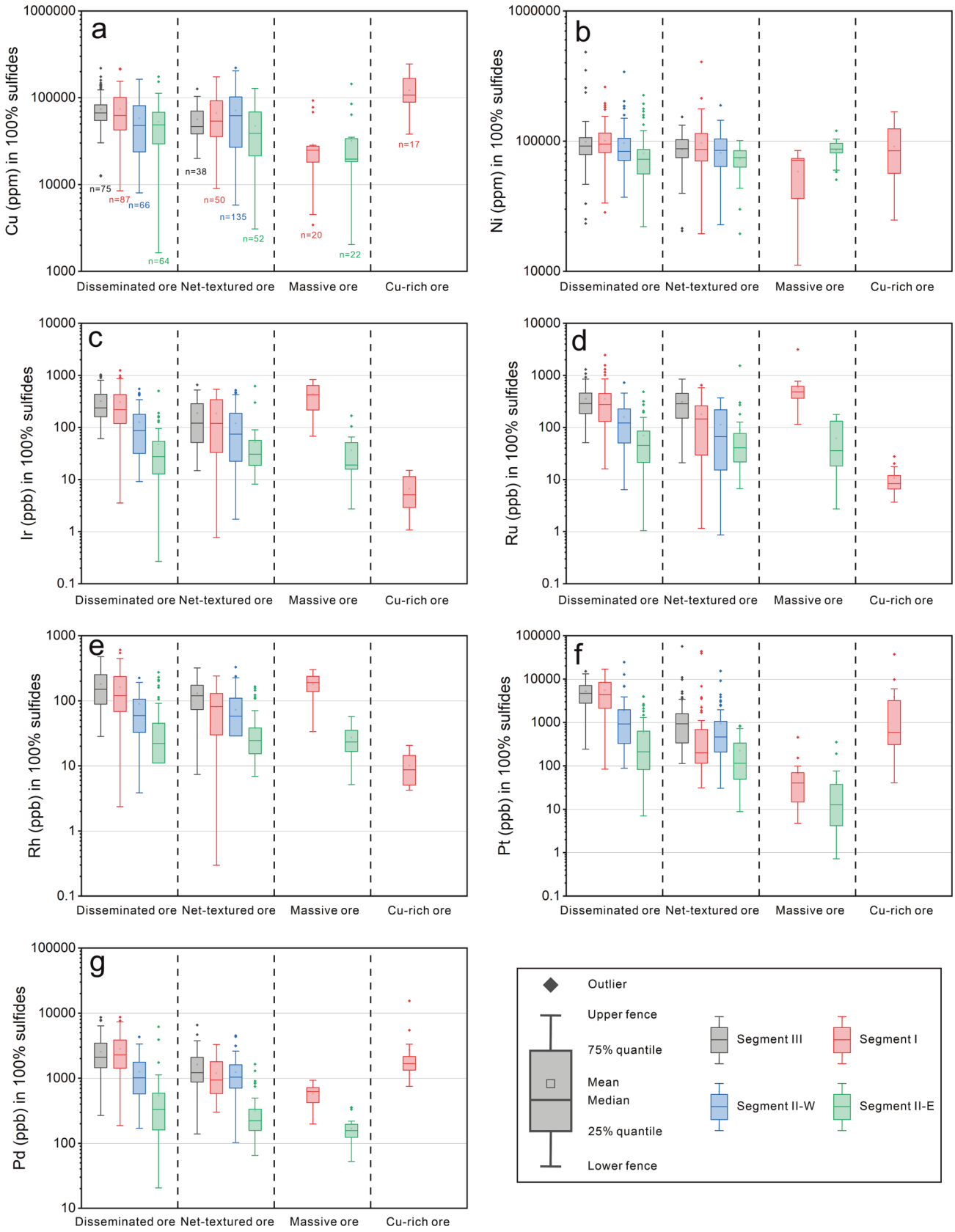

Fig. 7. Boxplots comparing Ni, Cu, and PGE tenors of disseminated, net-textured, massive, and Cu-rich ores in the Jinchuan deposit. Data sources as in Fig. 6.

have the highest Cu tenors, but their Ni tenors are similar to those of the disseminated and net-textured ores (Fig. 7a, b). Disseminated and net-textured ores show an overall decrease in PGE tenors from segments III–I, through Segment II-W, to Segment II-E (Fig. 7c–g); the change in PGE tenors is more apparent in the disseminated ores. Disseminated and net-textured ores in Segment II-E have the lowest PGE tenors of all the segments. Massive ore in Segment I has the highest Ir, Ru, and Rh tenors among all types of sulfide ores in the Jinchuan deposit, but its Pt and Pd tenors are generally lower than disseminated and net-textured ores (Fig. 7c–g). In contrast, massive ore in Segment II-E has Ir, Ru, and Rh tenors that are notably lower than those in disseminated, net-textured, and massive ores in the other three segments (Fig. 7c–e), with their Pt and Pd tenors being the lowest in the Jinchuan deposit (Fig. 7f, g). Copper-rich ores in Segment I have the lowest Ir, Ru, and Rh tenors among all types of sulfide ores (Fig. 7c–e), but their Pt and Pd tenors are similar to those of disseminated ores in segments III and I (Fig. 7f, g). It should also be noted that in segments III and I, Ir, Ru, Rh, Pt, and Pt tenors generally decrease from disseminated to net-textured ores; this is not observed in the other segments (Fig. 7c–g).

In summary, metal tenors of disseminated, net-textured, massive, and Cu-rich ores exhibit three types of variations. (1) For a given ore type, segments III and I have higher overall metal tenors than segments II-W and II-E. (2) Disseminated ores in segments III and I have higher overall metal tenors than net-textured ores, whereas the different ore types in segments II-W and II-E have indistinguishable metal tenors. (3) Massive ore in Segment I has relatively high IPGE tenors, but the lowest PPGE tenors, whereas Cu-rich ore in this segment has the lowest IPGE tenors, but relatively high PPGE tenors.

The relationships between Cu, Ni, and PGE tenors of the different ore types from segments III, I, II-W, and II-E are shown in Fig. 8. On a Cu tenor–Ni tenor plot, disseminated ores from the four segments exhibit a roughly positive correlation, whereas net-textured, massive, and Cu-rich ores exhibit a roughly negative correlation, with Ni/Cu ratios of 0.2–10 (Fig. 8a). All of the ore types together exhibit overall positive relationships between Pd–Pt tenors (Fig. 8b) and Ru–Ir tenors (Fig. 8c), with Pt/Pd and Ir/Ru ratios of 0.01–10 and 0.1–10, respectively (Fig. 8b, c). Disseminated ores, however, have slightly higher Pt/Pd ratios than the other types of sulfide ores, whereas Cu-rich ores have higher Ir/Ru ratios (Fig. 8b, c). On a Pd vs. Ir plot (Fig. 8d), disseminated ores exhibit an overall positive correlation, with Pd/Ir ratios of 1–100, whereas net-textured, massive, and Cu-rich ores display a broad negative correlation, with Pd/Ir ratios of 1–1000 (Fig. 8d). Net-textured, massive, and Cu-rich ores exhibit an overall negative correlation on a Ru tenor–Pd/Ru plot, but an overall positive correlation on a Pd tenor–Pd/Ru plot (Fig. 8e, f). Disseminated ores, however, display nearly vertical trends on both plots.

5.4. Primitive mantle-normalized metal patterns

Primitive mantle-normalized metal patterns for distinct ore types in segments III, I, II-W, and II-E are illustrated in Fig. 9. Disseminated ores in segments III and I are enriched in Pt–Pd–Cu relative to Ni–Ir–Ru, and have slight negative Ru and positive Pt anomalies (Fig. 9a, b). Disseminated ores in segments II-W and II-E exhibit a concave pattern and a pronounced positive Rh anomaly (Fig. 9d). Net-textured ores in the four segments exhibit significant negative Ir–Ru and positive Rh anomalies, with Pt anomalies ranging from positive to negative (Fig. 9a–d). Massive ores in segments I, II-W, and II-E have flat patterns from Ni to Rh and, apart from those in Segment III, display notably negative Pt anomalies (Fig. 9e). In contrast, Cu-rich ores in segments I display notably positive Pt anomalies (Fig. 9e).

5.5. Platinum-group element concentrations of pentlandite

Since most of the Pt concentrations in pentlandite are below or close to the detection limit, this element is not considered here. Furthermore, to avoid the 'nugget effect' from discrete PGMs on the analytical results of PGEs, time-resolved signals of all analyzed pentlandite spots were screened and only those showing generally flat patterns are considered (Fig. 10). The obtained PGE concentrations of pentlandite in sulfide ores from segments I, II-W, and II-E, together with previously published data, are compared in Fig. 11. The figure shows a generally decreasing trend in Os, Ir, Ru, Rh, and Pd concentrations of pentlandite from Segment I, through Segment II-W, to Segment II-E, which is similar to the variations in PGE tenors for a given sulfide ore type across these segments (Fig. 11).

6. Discussion

6.1. Controls on the metal tenors of different textural types of ore

The results presented here demonstrate that the different textural types of sulfide ores in the Jinchuan deposit are characterized by highly variable metal tenors. Given that the different ore types in the four segments have similar REE and trace-element patterns (ESM Fig. 3), the magmas from which the different ore types formed must be co-genetic, and so these metal-tenor variations are not related to the segregation of sulfide liquids from compositionally distinct parental magmas. Therefore, the variations in metal tenors should result from other mechanisms that formed or modified the mineralization; these mechanisms are discussed below.

6.1.1. Hydrothermal fluids

Interaction between magmatic sulfides and hydrothermal fluids may change the mineralogy of the sulfides and, thus, may have an effect on the metal tenors of the ores (Holwell et al., 2017; Brzozowski et al., 2023). For example, hydrothermal alteration can lead to the replacement of pyrrhotite and pentlandite by pyrite and millerite, respectively, resulting in the loss of Fe and S, as well as remobilization of base and precious metals (Mansur et al., 2021; Brzozowski et al., 2020; Brzozowski et al., 2023). The presence of abundant serpentine, chlorite, and tremolite in the host rocks of the deposit is direct evidence that hydrothermal fluids fluxed through these rocks. Three pieces of evidence highlight the influence of such fluids on the metal tenors of the sulfide ores. First, some disseminated and net-textured ores have S/Se ratios that are lower than the range of mantle values (Fig. 6g), which can be a result of S loss due to preferential remobilization of S over Se in hydrothermal fluids (Yamamoto, 1976; Queffurus and Barnes, 2015; Smith et al., 2016). Second, as observed in the disseminated ores (Fig. 4a–c), the coexistence of pyrite and magnetite within some pyrrhotite–pentlandite aggregates may result from oxidation of pyrrhotite by hydrothermal fluids via the reaction $4FeS\ (Po) + 2O_2 = FeS_2\ (Py) + Fe_3O_4\ (Mag) + S_2$ (Mansur et al., 2021). Third, Se-bearing PGM in the Jinchuan deposit have been found in association with carbonate, suggesting that Se and Pd were remobilized by hydrothermal fluids to some extent (Prichard et al., 2013). Despite the influence of fluids on metal tenors of sulfide ores in the Jinchuan deposit, given the similar variations between PGE tenors and PGE concentrations of pentlandite in sulfide ores across different segments of the Jinchuan deposit, PGE in sulfide ores should be primarily contained in magmatic sulfides (particularly pentlandite) (*cf.,* Chen et al., 2015), and so the calculated PGE tenors largely reflect the PGE contents of the sulfide liquids. The overall strong correlations between whole-rock Cu–Ni–Co–Se–PGE and S also indicate that the chalcophile elements in the Jinchuan deposit are primarily hosted by sulfides (Fig. 6a–g), principally pentlandite, pyrrhotite, and chalcopyrite. Additionally, while some samples exhibit S/Se ratios below the mantle range, the majority of samples have S/Se ratios that are within the range of mantle values (Fig. 6g), indicating that magmatic processes were the primary control on the S/Se ratios of sulfide ores (Queffurus and Barnes, 2015). Taken together, this indicates that the metal tenors of the sulfide ores were not significantly modified by hydrothermal fluids, at least not at the scale of hand sample.

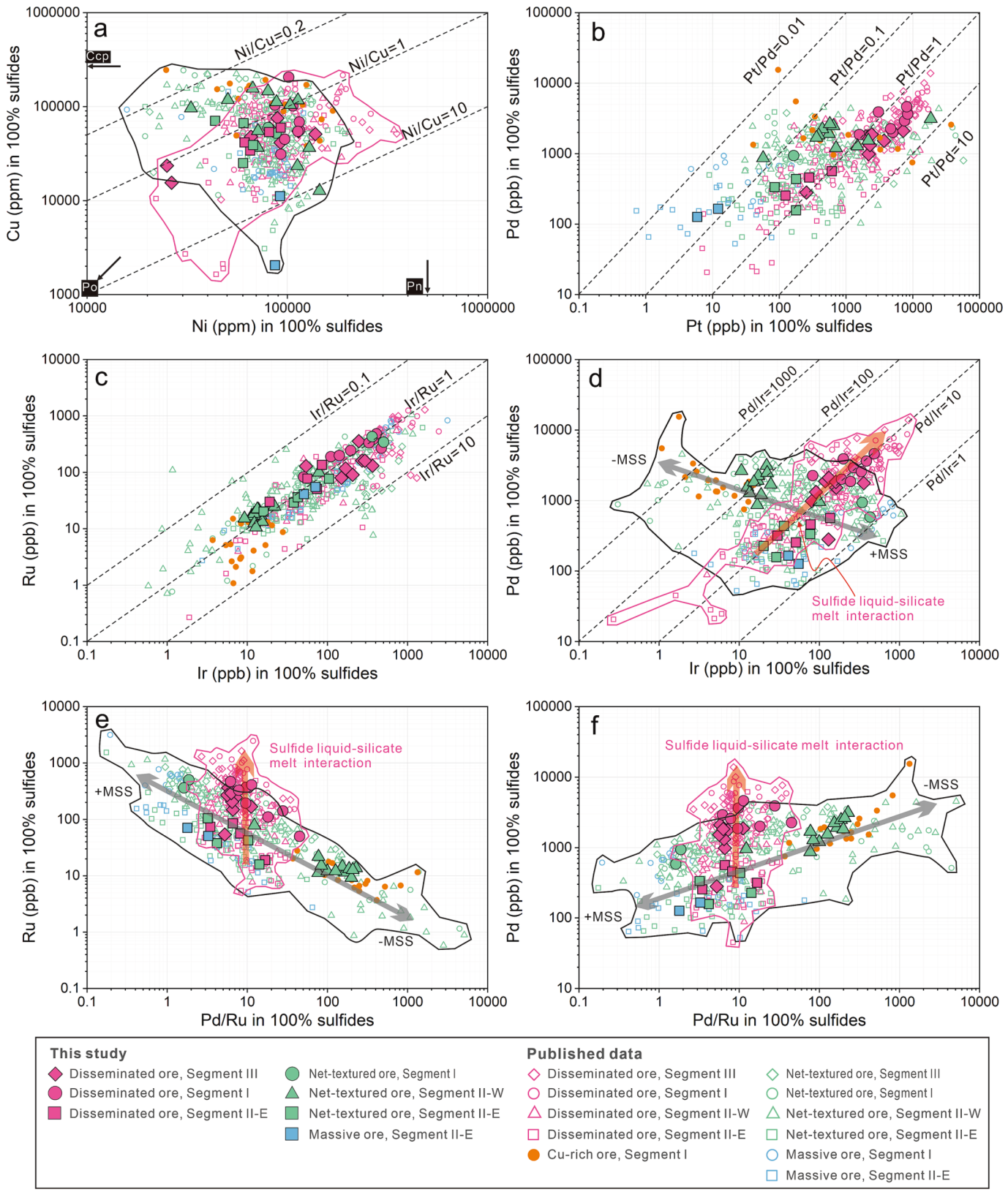

Fig. 8. Binary diagrams illustrating the variation between (a) Cu tenor and Ni tenor, (b) Pd tenor and Pt tenor, (c) Ru tenor and Ir tenor, (d) Pd tenor and Ir tenor, (e) Ru tenor and Pd/Ru, and (f) Pd tenor and Pd/Ru for disseminated, net-textured, massive, and Cu-rich ores in the Jinchuan deposit. The tenor of disseminated ores (outlined by a pink polygon) exhibits a distribution that is different from net-textured, massive, and Cu-rich ores (outlined by a black polygon). The reference lines for MSS fractionation and sulfide liquid–silicate melt interaction (*i.e.*, R factor) are from Kang et al. (2022); see text for more details. Data sources as in Fig. 6.

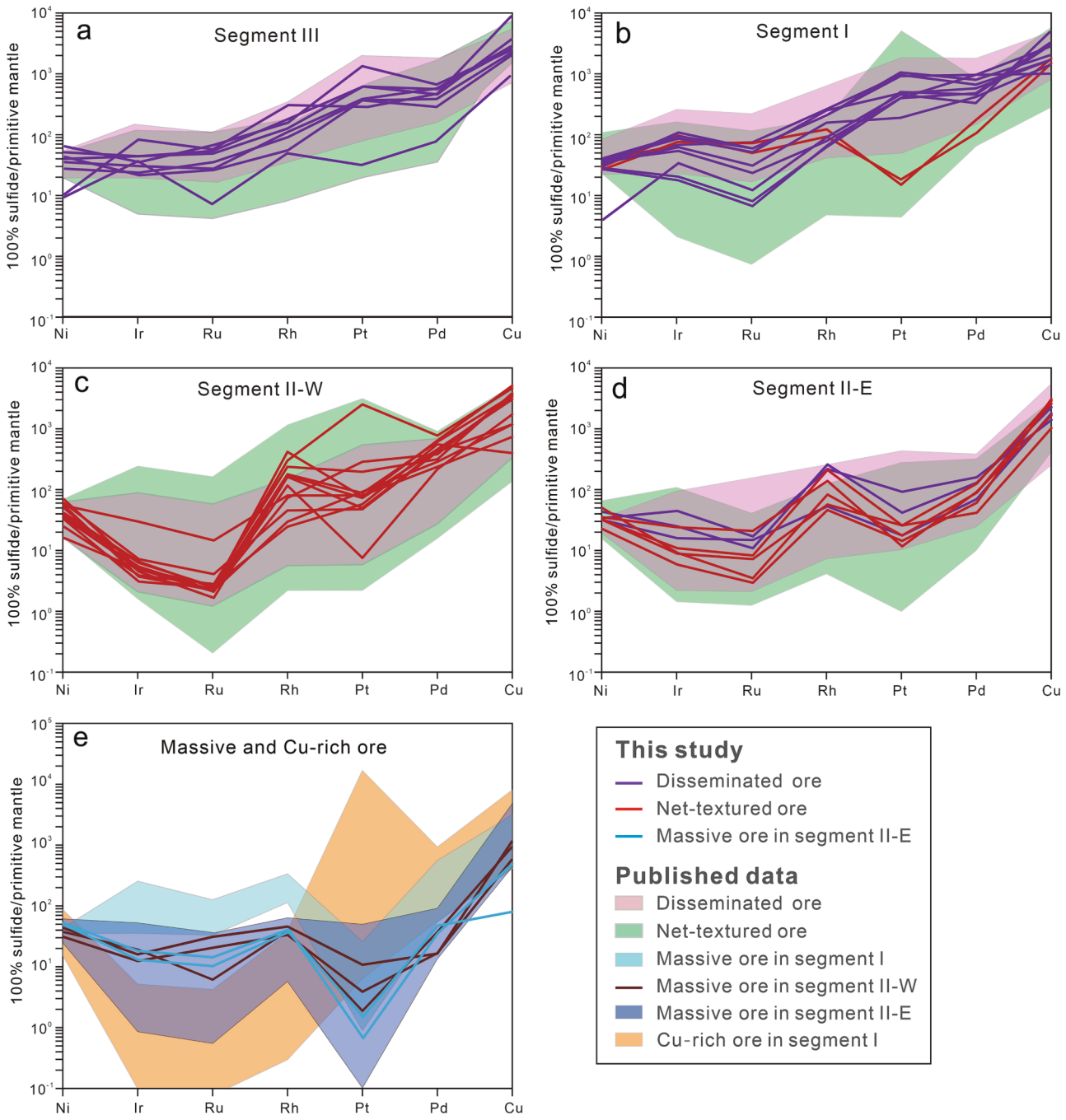

Fig. 9. (a–e) Primitive mantle-normalized Ni, Cu, and PGE composition (in 100% sulfide) of different ore types from different segments of the Jinchuan deposit. Normalization values are from McDonough and Sun (1995). The sources of published Jinchuan data as in Fig. 6.

6.1.2. Early crystallization of PGMs and the nugget effect of Pt alloys

Experimental results and natural samples have demonstrated that PGM can occur as liquidus phases in primitive melts at high temperatures and at a variety of redox conditions (Kamenetsky et al., 2015; Anenburg and Mavrogenes, 2016). It is, therefore, possible for PGMs to crystallize prior to the emplacement of mafic–ultramafic magmas, resulting in depletion of the PGEs in the residual magmas and negatively affecting the metal tenors of sulfide ores. In the Jinchuan deposit, the net-textured ore in Segment I, and massive ores in segments I and II-E are characterized by notably negative Pt anomalies (Fig. 9). Given the similar partition coefficients of Pd and Pt between sulfide liquids and silicate magmas (Li et al., 1996; Mungall and Brenan, 2014), the negative Pt anomalies may indicate the early precipitation of Pt alloys prior to sulfide saturation (Song et al., 2009; Chen et al., 2013). If so, it is expected that sulfide ores with pronounced negative Pt anomalies should have low Pt tenors. This is largely true given the observed low Pt tenors of net-textured ore in Segment I and massive ores in segments I and II-E (Fig. 7f). However, as reflected by the overall positive correlation between Pd and Pt tenors (Fig. 8b), ore samples with low Pt tenors also have low Pd tenors (Fig. 7g), which is difficult to reconcile by early precipitation of only Pt alloys. Additionally, the variations of Pt tenors for any specific type of ores across different segments of the Jinchuan deposit resemble those of other PGE tenors (Fig. 7). This observation is also difficult to be reconciled by early precipitation of only Pt alloys because variations of other PGE tenors are not affected by Pt alloys. Therefore, despite that early precipitation of Pt alloys may have

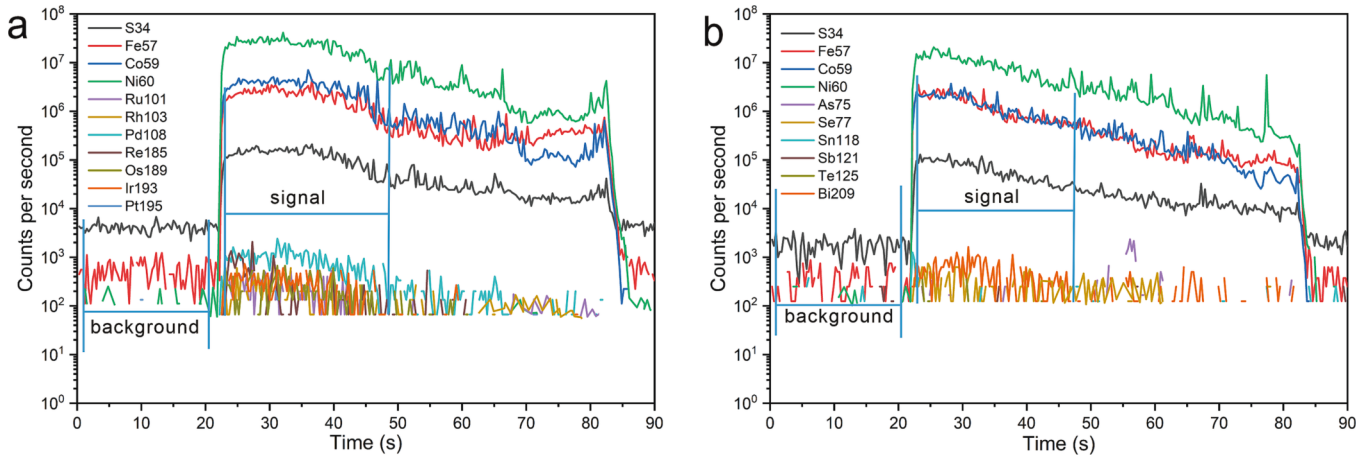

Fig. 10. Typical time-resolved spectra for LA-ICP-MS analyses of the pentlandite in the Jinchuan deposit.

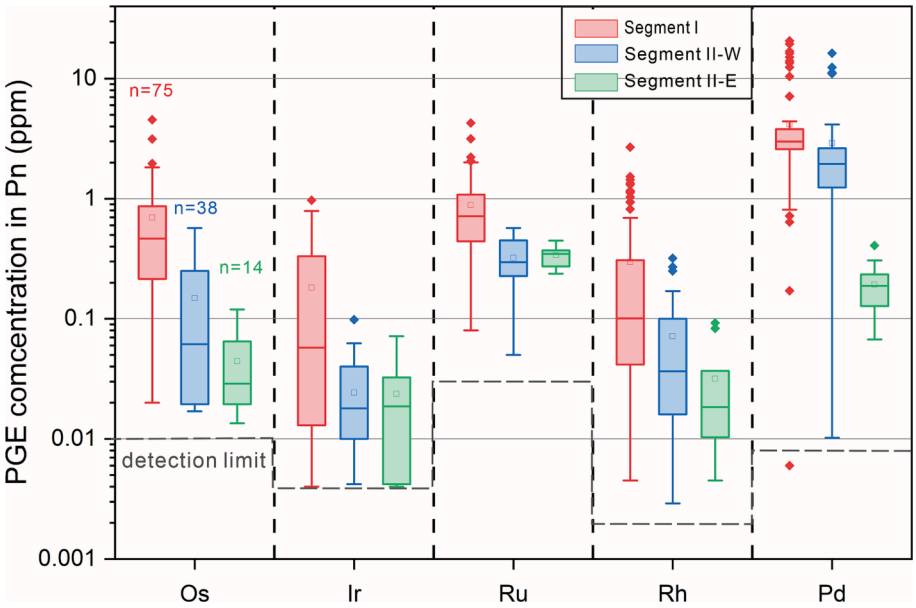

Fig. 11. Boxplots of PGE contents in pentlandite from different segments of the Jinchuan deposit, determined by LA-ICP-MS. Data sources: this study, Prichard et al. (2013), Chen et al. (2015), Han (2021), and Liang et al. (2022).

occurred, which would have decreased Pt tenors of some ore samples, the role of this process in controlling metal tenors was likely insignificant.

Another aspect that needs to be considered is that Pt is typically not hosted by sulfides in magmatic deposits, but mainly as Pt alloys (e.g., Pt-Fe alloy) (Li et al., 1996; Barnes et al., 2022). This results in a "nugget effect" that can affect Pt tenors due to heterogeneous distribution of Pt alloys (Barnes et al., 2022). The overall positive correlation between Pd and Pt tenors (Fig. 8b) suggest that Pt behaves similarly to Pd in the Jinchuan ore-forming system. As reflected by the positive relationship between Pd and S (Fig. 6f), Pd is dominantly controlled by sulfide liquids. Considering that Pt-S is also positively correlated (Fig. 6e), Pt alloys, if any, also likely crystallized from sulfide liquids. In this context, the calculated Pt tenors reflect the Pt concentrations of the sulfide liquids, despite the possible presence of Pt alloys in the samples. It is reasonable to expect that, if the variation of Pt tenors is related to the 'nugget effect', then for a specific type of sulfide ore from a given segment of the Jinchuan deposit, the variation of Pt tenors would be greater than that of other PGE tenors due to the heterogeneous distribution of Pt alloys within the ore. However, this is not the case as Pt tenors exhibit similar degrees of variation with other PGE tenors for a specific type of sulfide ore in a given segment (Fig. 7). This similarity suggests that the 'nugget effect' on Pt tenor variations is likely insignificant, which is reasonable given the large population of samples that was used for the metal tenor calculations that would have mitigated the influence of the nugget effect (*cf.*, Barnes et al., 2022).

6.1.3. *Early sulfide removal*

Sulfide liquids that exsolve from silicate magmas scavenge and concentrate metals that are present in the magmas. Therefore, removal of sulfide liquid prior to emplacement of an intrusion will inevitably deplete the residual magmas in metals and, thus, negatively influence metal tenors. As Pd is more chalcophile than Cu (Mungall and Brenan, 2014), early sulfide removal will deplete the Pd content of magmas to a greater degree than Cu, resulting in elevated Cu/Pd ratios in residual magmas. Ore samples from segments III, I, II-W, and II-E have Cu/Pd ratios that are generally higher than mantle values (1000–10,000; Barnes et al., 2015) (Fig. 6h), indicating that the magmas from which the four segments crystallized likely lost sulfide liquid. This is supported by the degree of early sulfide removal estimated through modeling

variations in whole-rock Cu/Pd ratios (ESM Text S1 and ESM Fig. S4). Higher degrees of sulfide removal will undoubtedly result in lower metal tenors in the sulfide ores that form from the residual magmas. Ores in segments III and I, which experienced lower degrees of sulfide removal (~0.0025 % and ~ 0.003 %), have higher overall metal tenors than ores in segments II-W and II-E, which experienced the highest degree of sulfide removal (~0.0035 % and ~ 0.0045 %) and have the lowest metal tenors in general (Fig. 7). It is, therefore, suggested that at least some of the observed variations in metal tenors in a given textural type of ore across the four segments was controlled by variable degrees of early sulfide removal.

6.1.4. *R factor and fractionation of sulfide liquids*

Interaction between sulfide liquid and magma (*i.e.*, R factor) is an important control on the chalcophile element content of base-metal sulfides, with high R factors generating high chalcophile element concentrations in sulfide liquids and, thus, high metal tenors in sulfide ores (Barnes and Lightfoot, 2005). Fractionation of sulfide liquids produces Fe-rich MSS and residual Cu-rich residual liquids, the latter of which crystallizes to intermediate solid solution (ISS) (Naldrett et al., 1967). Since Ni and the IPGE are mildly and strongly partitioned into MSS (e.g., $D_{Ni}^{MSS/Sul}$ = 0.36–1.72, $D_{Ir}^{MSS/Sul}$ = 2.3–14.7; Barnes and Ripley, 2016), respectively, whereas Cu and the PPGE are strongly partitioned into the residual Cu-rich liquid (e.g., Li et al., 1996; Mungall et al., 2005), fractionation of sulfide liquids can potentially lead to the fractionation of metals within a deposit (e.g., if the MSS and ISS were physically separated), affecting the metal tenors of the resultant sulfide ores.

The composition of disseminated sulfides is likely to have been less affected by sulfide liquid fractionation due to their occurrence interstitial to silicate minerals; disseminated sulfides may, therefore, retain their original sulfide liquid composition, which varied as a function of R factor (Duran et al., 2017; Li and Mungall, 2022). Disseminated sulfide ores in the Jinchuan deposit display well-defined positive correlations between whole-rock Cu–Ni–Co–Ru–Pt–Pd and S (Fig. 6a–f), and relatively invariable Pd/Ru ratios with increasing Ru and Pd tenors (Fig. 8e–f). Both of these features indicate that the PPGE, IPGE, Ni, Co, and Cu contents of disseminated ores did not fractionate with evolution of the sulfide liquids. The metal tenors of this ore type are, therefore, representative of the composition of the original sulfide liquids, which varied as a result of varying R factor (Duran et al., 2017). In contrast, net-textured, massive, and Cu-rich sulfide ores define steeper correlations between whole-rock Cu–Ni–Co–Ru–Pt–Pd and S (Fig. 6a–f), indicating that the composition of sulfides in these ore types are related to the physical fractionation/separation of MSS and ISS from the evolving sulfide liquids (Duran et al., 2017). Furthermore, the well-defined negative correlation between Ru tenor and Pd/Ru ratio, and positive correlation between Pd tenor and Pd/Ru ratio for net-textured, massive, and Cu-rich ores highlights the decoupling of Pd and Ru (Fig. 8e, f), which is typical of ores that crystallized from fractionated sulfide liquids given the contrasting geochemical affinity of Pd and Ru for MSS and ISS (Li et al., 1996; Barnes et al., 2016).

Metal variations as a function of R factor and sulfide liquid fractionation were modeled to assess the relative importance of these processes in controlling the metal tenors of the ores. The equation of Campbell and Naldrett (1979) was used to model variations in Pd and Ir tenors as a function of R factor, where the concentrations of Pd and Ir in the silicate melt were calculated based on the degree of sulfide removal in each segment (see ESM Text S1), and the partition coefficients of Pd–Ir between sulfide liquid–silicate melts ($D_{Pd,Ir}^{Sul/Sil}$) and MSS–sulfide liquid ($D_{Pd,Ir}^{MSS/Sul}$) (partition coefficient data from Barnes and Ripley, 2016); details of the modeling parameters are provided in Table 2. As silicate melts in different segments experienced different degrees of sulfide removal, it is not surprising that the concentrations of Pd and Ir in the silicate melts used in the models are different (Table 2), despite the fact that the parental magmas from which the different segments formed are co-genetic (ESM Fig. 3). Variations in the metal tenors of disseminated ores in each segment follow the R factor model curves, with R factors being in the range of 1,000–50,000 in segments III and I, and 1,000–10,000 in segments II-W and II-E (Fig. 12). These values are in agreement with those estimated by Song et al. (2009) and Long et al. (2023), who suggested that the minimum R factor was close to 1000. Other authors, however, suggested that the minimum R factor was close to 100 (Li and Ripley, 2011; Chen et al., 2013; Duan et al., 2016). There are likely two reasons for this discrepancy: i) consideration of the effects of early sulfide removal on the starting silicate melt composition and ii) the choice of the $D_{Pd,Ir}^{Sul/Sil}$ values. The latter R factor simulations utilized higher initial values of Pd–Ir for the initial silicate melt than this study and lower $D_{Pd,Ir}^{Sul/Sil}$ values of 30,000 and 40,000 (Peach et al., 1994), respectively, all of which would lead to lower R factor estimates. As the R factor simulations in this study considered the effects of early sulfide removal on the starting silicate melt composition, and also used recently reported $D_{Pd,Ir}^{Sul/Sil}$ values, the R factors estimates obtained here are considered reliable. Based on the modeling results, it is suggested that the higher metal tenors of the disseminated ores compared to the net-textured ores in segments III and I can be attributed to the differences in R factor experienced by their respective sulfide liquids (*i.e.*, sulfides that comprise the disseminated ores generally experienced higher R factors than those that comprise the net-textured ores) (Fig. 12a, b). The overall similarity in metal tenors of disseminated and net-textured ores in segments II-W and II-E, however, can be attributed to the comparable R factors experienced by their respective sulfide liquids (Table 2, Figs. 7, 11, 12c–d).

The metal tenors of the net-textured, massive, and Cu-rich ores in these segments largely fall between the MSS and fractionated liquid model curves (Fig. 12). This indicates that variations in the metal tenors of these ores in each segment are principally controlled by sulfide liquid fractionation, although metal variations caused by R factor likely also played a role. The modeling results also demonstrate that the massive ores in segments I and II-E experienced notably lower degrees of sulfide liquid fractionation (F = 1.0–0.8, F is the fraction of residual sulfide liquid) than the net-textured ores (F = 0.8–0.4), with metal tenors generally plotting closer to the MSS model curve compared to the net-textured ores (Fig. 12b, d). Accordingly, the massive ores represent accumulations of MSS, with minor amounts of trapped Cu-rich liquid, consistent with their overall mineralogy (Fig. 6, Duran et al., 2017). Given that the IPGE are compatible into MSS and the PPGE are incompatible (Li et al., 1996; Ballhaus et al., 2001; Mungall et al., 2005), the early formed MSS cumulates should preferentially concentrate the IPGE, such that the massive ores should have the highest IPGE tenors and lowest PPGE tenors among all of the ore types, even though their sulfide liquids experienced lower R factors than the disseminated ores, which is observed (Fig. 7, 12b, d). The Cu-rich ores in Segment I experienced higher degrees of sulfide liquid fractionation (F = 0.5–0.3) and have metal tenors that plot closer to the fractionated liquid model curve than the other types of ores (Fig. 12b), indicating that this ore type likely formed from residual Cu-rich liquid. The presence of Cu-rich veins along fractures through the marble country rock is consistent with the low melting temperature (*e.g.*, <800℃) and mobile nature of residual Cu-rich liquids (Fig. 3e) (Craig and Kullerud, 1969; Barnes et al., 2018). Since the PPGE are compatible into residual Cu-rich liquid and the IPGE are not (Li et al., 1996; Ballhaus et al., 2001), the low IPGE and high PPGE tenors of this ore type likely result from the fact that it represents the fractionated portion of the sulfide liquid (Fig. 7c–g).

6.2. *Quantifying metal enrichment processes in the Jinchuan deposit*

It is widely accepted that the Jinchuan deposit formed by multiple injections of sulfide-laden, high-Mg basaltic magma in a dynamic magma conduit system followed by concentration of this sulfide liquid (Chai and Naldrett, 1992a; Song et al., 2009, 2012; Tonnelier, 2010; Chen et al., 2013; Duan et al., 2016). Quantifying the contribution of multiple magmatic pulses to metal enrichment in the different segments

Table 2
Modeling of Pd and Ir tenors as a function of variable R factor and different degrees of sulfide liquid fractional crystallization.

Segment	Segment III				Segment I				Segment II-W				Segment II-E			
$D_{Pd}^{Sul/Sil}$	100,000															
$D_{Ir}^{Sul/Sil}$	100,000															
$D_{Pd}^{MSS/Sul}$	0.1															
$D_{Ir}^{MSS/Sul}$	5															
(1) R-factor model																
X_0^{Pd} (ppb)	0.74				0.45				0.27				0.1			
X_0^{Ir} (ppb)	0.08				0.05				0.03				0.01			
	X_L^{Pd}	X_L^{Ir}			X_L^{Pd}	X_L^{Ir}			X_L^{Pd}	X_L^{Ir}			X_L^{Pd}	X_L^{Ir}		
R = 1	0.74	0.08			0.45	0.05			0.27	0.03			0.10	0.01		
R = 10	7.40	0.80			4.50	0.50			2.70	0.30			1.00	0.10		
R = 100	73.93	7.99			44.95	4.99			26.97	3.00			9.99	1.00		
R = 1000	732.7	79.21			445.5	49.50			267.3	29.70			99.01	9.90		
R = 10,000	6,727	727.3			4,091	454.5			2,455	272.7			909.1	90.91		
R = 100,000	36,999	3,999			22,500	2,500			13,5000	1,500			5,000	500.1		
(2) Fractional crystallization model																
R value	3000				3000				8000				5000			
C_0^{Pd} (ppb)	2,155				1,311				2,000				476			
C_0^{Ir} (ppb)	233				146				222				48			
	C_L^{Pd}	C_L^{Ir}	C_S^{Pd}	C_S^{Ir}	C_L^{Pd}	C_L^{Ir}	C_S^{Pd}	C_S^{Ir}	C_L^{Pd}	C_L^{Ir}	C_S^{Pd}	C_S^{Ir}	C_L^{Pd}	C_L^{Ir}	C_S^{Pd}	C_S^{Ir}
F = 1	2,155	215.5	233.01	1,165	1,311	131.1	145.63	728.15	2,000	200.0	222.2	1,111.1	476.19	47.62	47.62	238.09
F = 0.9	2,370	237.0	152.9	764.5	1,441	144.1	95.55	477.74	2,199	219.9	145.8	729.0	523.5	52.35	31.24	156.21
F = 0.8	2,635	263.5	95.44	477.2	1,602	160.2	59.65	298.25	2,445	244.5	91.02	455.11	582.1	58.21	19.50	97.52
F = 0.7	2,971	297.1	55.95	279.7	1,807	180.7	34.97	174.83	2,757	275.7	53.36	266.78	656.4	65.64	11.43	57.17
F = 0.6	3,413	341.3	30.20	151.0	2,076	207.6	18.87	94.37	3,167	316.7	28.80	144.00	754.1	75.41	6.17	30.86
F = 0.5	4,022	402.2	14.56	72.81	2,446	244.6	9.10	45.51	3,732	373.2	13.89	69.44	888.5	88.86	2.98	14.88
F = 0.4	4,917	491.7	5.96	29.82	2,990	299.0	3.73	18.64	4,562	456.2	5.69	28.44	1,086.2	108.6	1.22	6.10
F = 0.3	6,369	636.9	1.89	9.44	3,873	387.3	1.18	5.90	5,910	591.1	1.80	9.00	1,407.2	140.7	0.39	1.93
F = 0.2	9,175	917.5	0.37	1.86	5,579	557.9	0.23	1.17	8,513	851.3	0.36	1.78	2,027	202.7	0.08	0.38
F = 0.1	17,120	1,712	0.02	0.12	10,411	1,041	0.01	0.07	15,886	1,589	0.02	0.11	3,783	378.3	0.00	0.02

Note: $D_{Pd,Ir}^{Sul/Sil}$: partition coefficient of an element between sulfide liquid and silicate melt, $D_{Pd,Ir}^{MSS/Sul}$: partition coefficient of an element between MSS and sulfide liquid, X_0: concentration of an element in the initial silicate magma, X_L: concentration of element in the sulfide liquid, C_0: original sulfide liquid composition at a given R factors, F: remaining fraction of sulfide liquid, C_L: concentration of an element in the silicate melt, and C_S: concentration of an element in MSS. The concentration of Pd and Ir in the starting silicate melt for the R factor model were calculated based on the degree of early sulfide removal in each segment (See Table S1 in ESM Text S2). The partition coefficient of elements was obtained from Barnes and Ripley (2016). See text for more information.

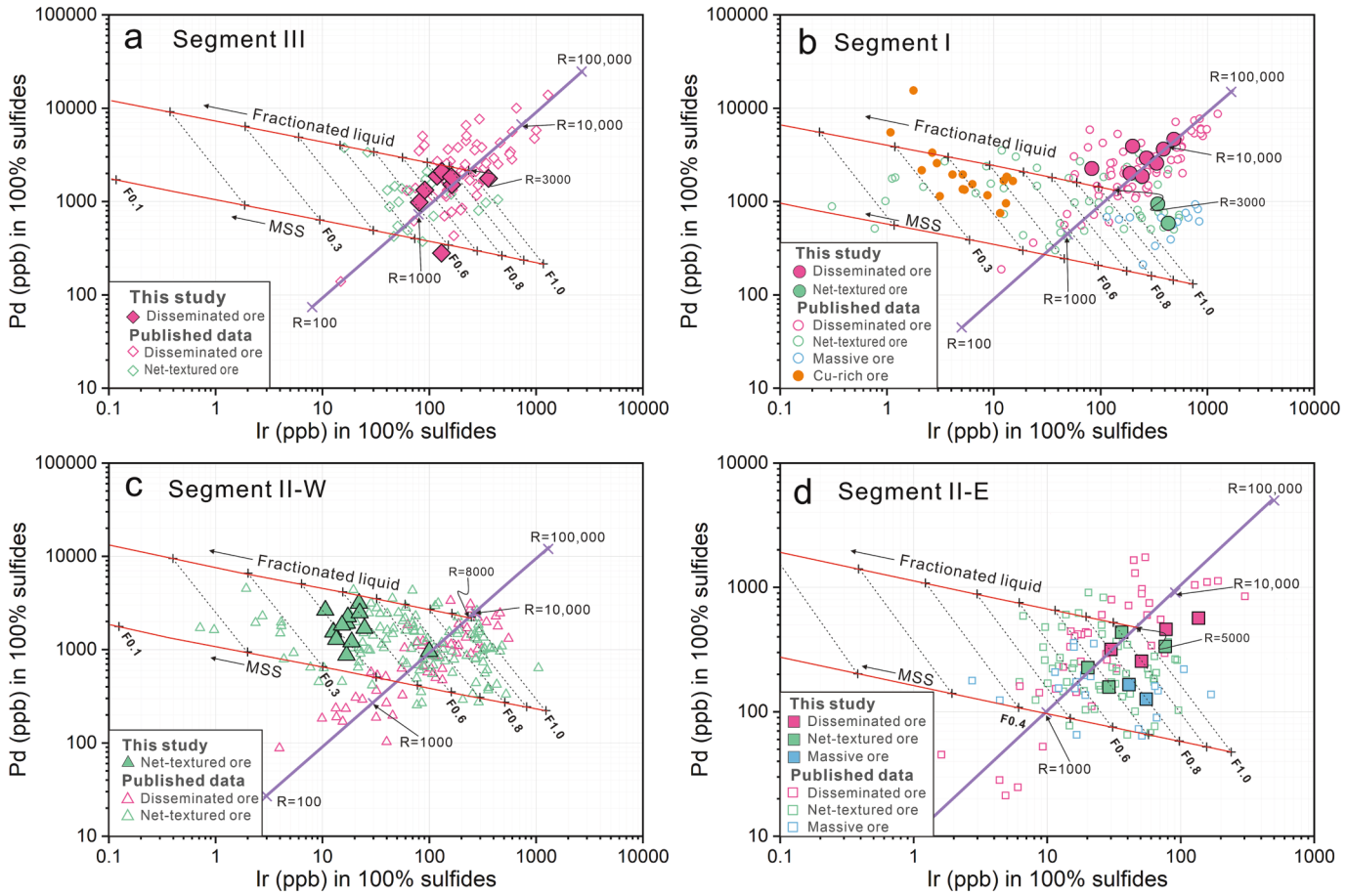

Fig. 12. Numerical models illustrating the variation in Pd and Ir tenors as a result of variations in R factor and fractional crystallization of sulfide liquid. Partition coefficients: $D_{Pd,Ir}^{Sul/Sil} = 100{,}000$, $D_{Ir}^{MSS/Liq} = 5$, $D_{Pd}^{MSS/Liq} = 0.1$. Data sources as in Fig. 6.

of the Jinchuan deposit is crucial for examining the physicochemical dynamics of different portions of the conduit system.

Based on the relationship between Pd and Ir tenors, the maximum R factor required to attain the PGE tenors of some of the disseminated ores is estimated to have been up to ~ 100,000 (Fig. 12), similar to the R factors experienced by sulfide liquids that form other PGE-rich mineralization (Brzozowski et al., 2020). This maximum R factor is likely attainable in a flow-through (conduit) system whereby sulfide liquids interacted with large volumes of magma through multiple recharge events (Maier et al., 2001; Kerr and Leitch, 2005). Given that early sulfide removal may have resulted in the formation of pools of sulfide liquid at depth, metal enrichment likely occurred via a mechanism similar to that described by Robertson et al. (2016). This mechanism, which was also suggested by Brzozowski et al., (2020), Brzozowski et al. (2021a), Brzozowski et al. (2021b) for the Marathon deposit, involves the passage of magma over, and interaction with, pools of sulfide liquid, resulting in variable degrees of metal enrichment in the sulfide liquids depending on the extent of time in which the sulfide pool interacted with the magma (*i.e.,* sulfide droplets mobilized from the pool early will have lower metal tenors than those mobilized from the pool after longer periods of time). We quantitatively assessed this mechanism using the equation described by Cao et al. (2021), which is an updated version of the multistage dissolution upgrading equation of Kerr and Leitch (2005):

$$C_{WR} = Xo^{*}\left(\frac{DR'_{inc}}{R'_{inc} - LD}\right) \times \left[1 - \left(\frac{D}{R'_{inc} + D - LD}\right)^{N}\right]^{*} C_{Sulfide}$$

where C_{WR} is the whole-rock concentration of a given metal (Cu and Se: ppm; Pd: ppb), X_0 is the initial metal concentration in the magma (unit is the same as C_{WR}), R'_{inc} is the incremental R factor that represents the mass of each individual magma batch divided by the mass of the remaining sulfide liquid, L is the incremental dissolution rate or 'loss factor' that represents the proportion of sulfide liquid (in wt. %) dissolved by each successive magma batch, N is the number of magma batches that interacted with the sulfide pool, D is the sulfide liquid–silicate melt partition coefficient for a given metal, and $C_{Sulfide}$ is the estimated amount of sulfide in a rock (in wt. %).

We followed the protocol of Cao et al. (2021) to select appropriate parameters for modeling the C_{WR} of the Jinchuan ore samples. Only the C_{WR} of the disseminated ores was modeled because the metal tenors of this ore type are principally controlled by R factor and largely unaffected by other processes (e.g., sulfide liquid fractionation) (Fig. 12). According to Fig. 12 and previous studies (Song et al., 2009; Long et al., 2023), the maximum R factor was set to 100,000, and the partition coefficients used for Pd–Ir are the same as those described earlier (Table 2). Other parameters include $D_{Se}^{Sul/Sil} = 2000$, $R'_{inc} = 300$, and $L = 0.4$. Details of the modeling and the parameters are provided in ESM Text S2. As shown in ESM Fig. 5, using these parameters allows the maximum R factor to be reached using the minimum number of magma batches (*N*). Although the range of each variable is considered reasonable, the variables were chosen to minimize the number of pulses required to solve the model, thereby improving its geological plausibility (*cf.,* Cao et al., 2021). The model curves in Fig. 13 illustrate the variability in whole-rock Cu, Pd, and Se concentrations as a result of multi-stage dissolution upgrading at different R factors, and at sulfide contents of 0.1 wt%, 0.5 wt%, 1 wt%, and 5 wt%. This modeling demonstrates that, with increasing R factor, sulfide liquid is continuously consumed, decreasing the fraction of sulfide liquid remaining (*f*) in the pool (Fig. 13). The success of this model is

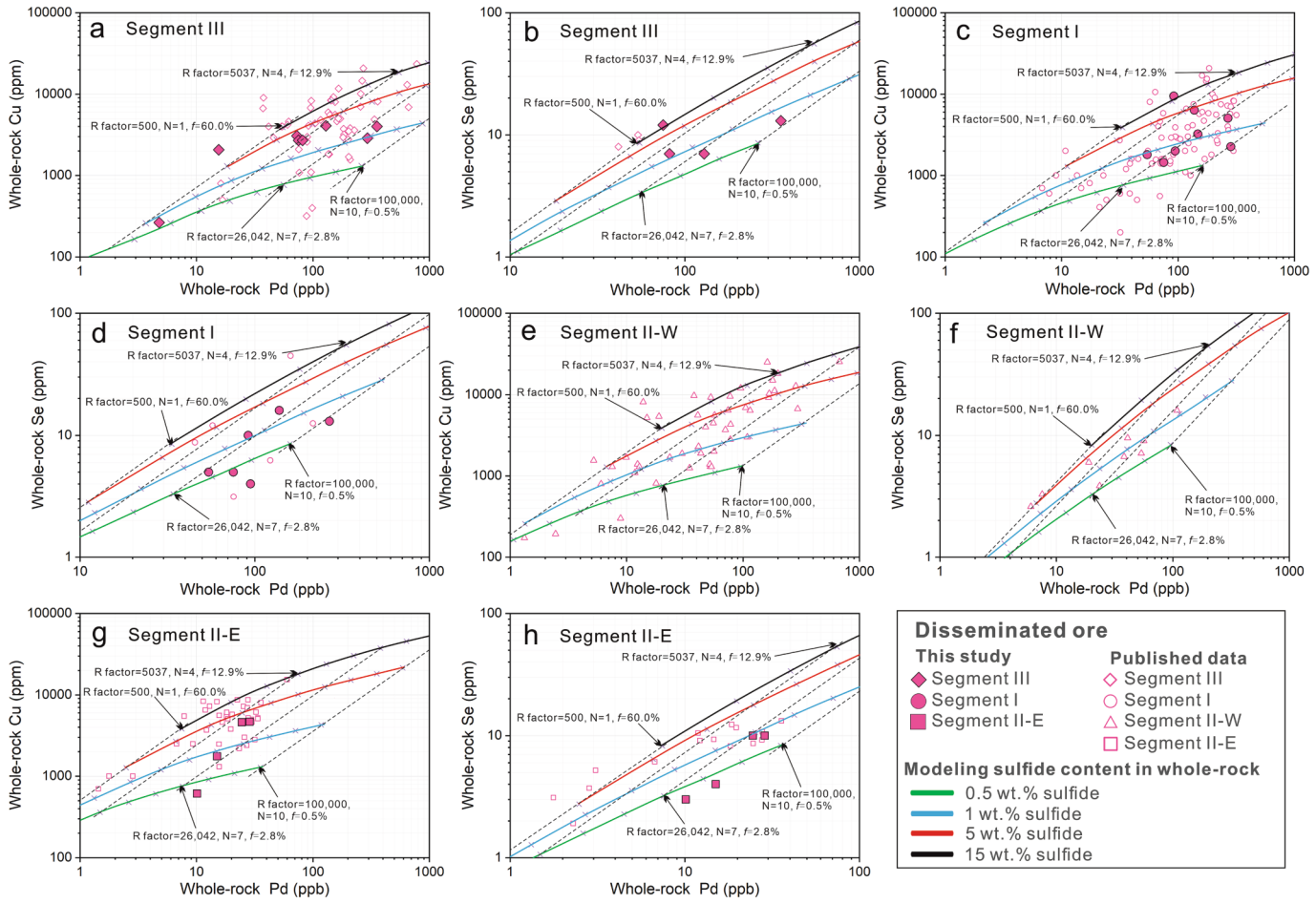

Fig. 13. Model curves illustrating the variation in bulk-rock Cu, Se, and Pd as a function of multistage dissolution upgrading and different amounts of sulfide liquid (0.5 wt%, 1 wt%, 5 wt%, and 15 wt% sulfides). The composition of disseminated ores in the four segments are provided for comparison to the model curves. The R factor of each magma batch (R'_{inc}) was set to 300 and the sulfur loss factor (L) was set to 0.4. The X's on the model curves are the R factor. The dashed lines connecting the X's on the model curves illustrate the change in whole-rock chalcophile element abundances as a function of the amount of sulfide liquid at a given R factor. Data for disseminated sulfide ores are provided for comparison to the model curves. See text for more details.

demonstrated not only by how well the whole-rock metal values match the model curves (Fig. 13), but also by the agreement between modeled sulfide abundances and the actual amount of sulfides in the rocks (Fig. 14).

The results show that disseminated ores in segments III and I could have formed by interaction of sulfide liquid with up to 10 batches of magma, with R factors of less than 100,000; the fraction of sulfide liquid remaining (f) would have been in the range of 60–0.5 % (Fig. 13a–d). Disseminated ores in segments II-W and II-E, however, could have formed by interaction of sulfide liquid with up to 7 batches of magma, with R factors of less than 30,000; the fraction of sulfide liquid remaining (f) would have been in the range of 60–2.8 % (Fig. 13e–h). This modeling, therefore, provides a basis to evaluate the physico-chemical dynamics of magma conduits. For example, the greater number of magma batches in segments III and I compared to segments II-W and II-E suggest that the portions of the conduit system in the former two segments were likely more dynamic than in the latter two segments. Additionally, the model also shows that the low sulfide content of some orebodies at Jinchuan may be the result of dissolution rather than simply low initial volumes of sulfide liquid.

6.3. *Implications for the formation of different ore types in magma conduits*

Sulfide liquid is largely transported by magma in the form of dispersed droplets (Robertson et al., 2015; Yao et al., 2019; Yao and Mungall, 2022). In dynamic conduit systems, sulfide droplets may become smaller in size either due to continued dissolution by the influx of S-undersaturated magmas (Kerr and Leitch, 2005) or by physical break-up in chaotic laminar flows (Robertson et al., 2016). Sulfide-laden magma flowing through a widening conduit may result in coarser blebs settling out of the magma under the force of gravity, leading to the percolation and accumulation of sulfide liquids, and formation of net-textured and massive sulfide ores (Yao et al., 2019). The finer sulfide droplets, however, may remain suspended in the flowing magmas; during solidification of the magma in shallow crustal reservoirs, these finely dispersed droplets of sulfide liquid crystallize to form disseminated ores (Robertson et al., 2015, 2016). Alternatively, small sulfide droplets may coalesce to form interconnected, net-textured domains, particularly when magma flow is stagnant. Thus, coalescance and interpore drainage of originally disseminated sulfides in mush zones may also be important in the generation of disseminated and net-textured ores, and even massive ores, through extensive sulfide accumulation (Barnes et al., 2017; Mao et al., 2018).

Disseminated ores in segments III and I of the Jinchuan deposit represent sulfide liquids that formed at higher R factors than the sulfide liquids that formed the associated net-textured and massive ores (Fig. 12a, b). This indicates that sulfide liquids that formed the disseminated ores may have remained in suspension after the formation of the net-textured and massive ores, providing it with a longer

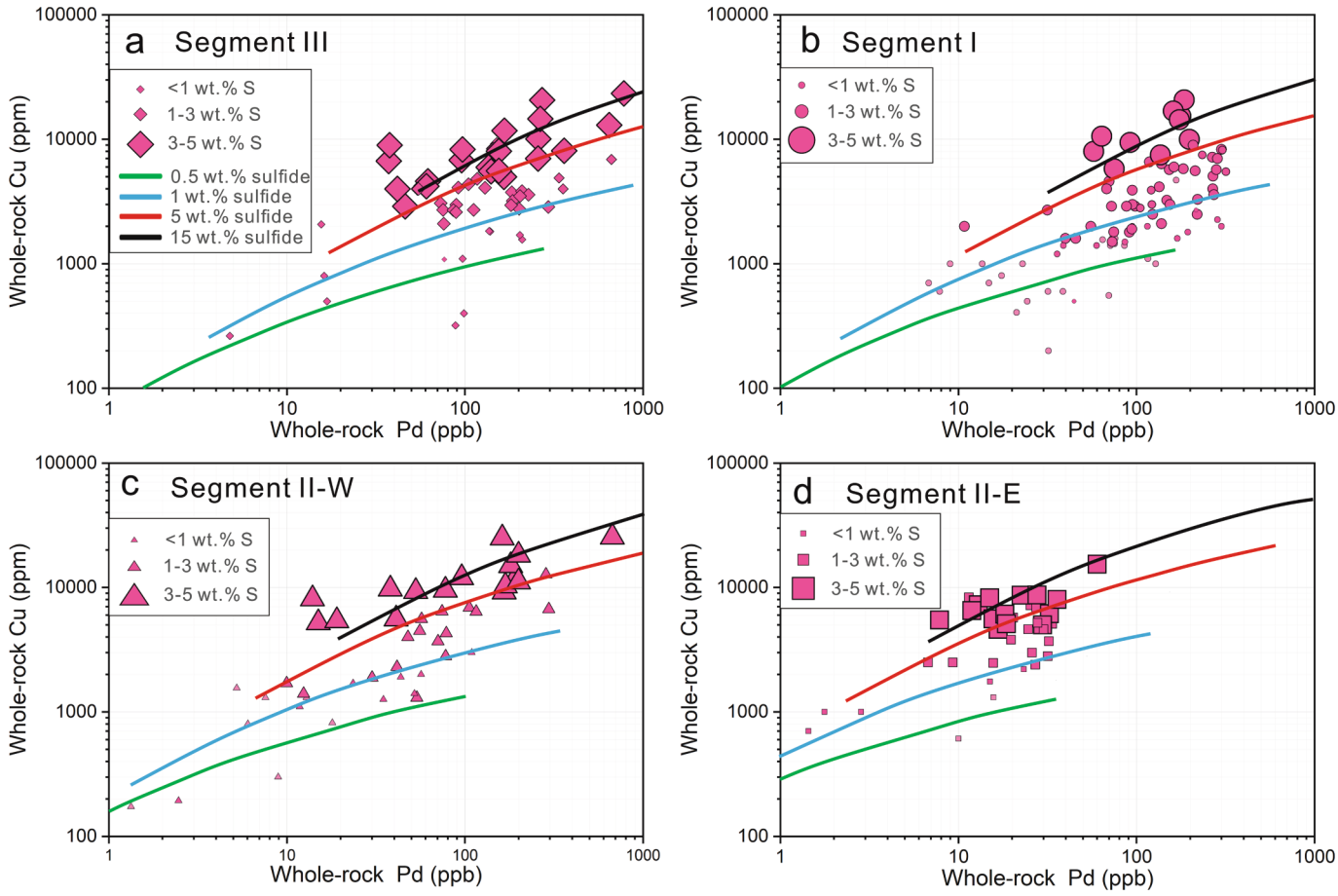

Fig. 14. Binary diagrams illustrating the modeled variation in whole-rock Cu and Pd contents as a function of multistage dissolution upgrading and different amounts of sulfide. The size of the data points corresponds to the whole-rock S content of the disseminated ores. The amount of sulfide estimated by the model curves agrees well with the observed abundances of sulfide in the samples.

opportunity to interact with magmas. Such a scenario can be achieved if the sulfide liquids represented by the disseminated ores experienced higher degrees of dissolution upgrading and/or break-up via dynamic magma flow, which led to the formation of finer droplet sizes. This decrease in droplet size, in combination with a decrease in sulfide liquid volume, ultimately enhanced its ability to be carried by magmas (Fig. 13) (Kerr and Leitch, 2005; Robertson et al., 2016). This mechanism is not only consistent with the spatial distribution of the different types of mineralization in these two segments (*i.e.,* the disseminated ores are mostly located in the upper portions of the net-textured ores) (Chen et al., 2013; Kang et al., 2022), but also consistent with the suggestion by Kang et al. (2022) that disseminated sulfides in Segment III remained in diffuse contact with the above flowing magma, resulting in the elevated PGE tenors. We, therefore, consider that net-textured and massive sulfide ores in segments III and I formed via early percolation and accumulation of finely dispersed sulfide droplets carried from depth. Some sulfide droplets, which ultiamtely experienced greater R factors, remained in suspension and eventually crystallized within the cumulate pile (e.g., olivine, clinopyroxene) higher up in the section, forming the disseminated ores in the two segments.

In segments II-W and II-E, disseminated ores formed from sulfide liquids that experienced R factors similar to that of the sulfide liquids that formed the net-textured and massive ores (Fig. 12c, d). This suggests that the varying amounts of sulfide in these ore types is likely related purely to mechancial settling processes rather than dissolution related to sulfide liquid–silicate melt interaction. Such a scenario can be achieved by the aforementioned 'sulfide percolation' model, whereby originally disseminated sulfides migrated through inter-crystal pore space under the force of gravity and coalesced, forming either a network of sulfide liquid by displacing interstital silicate melt in a mush zone or massive ore by extensive accumulation of sulfide droplets (*cf.,* Barnes et al., 2017). Here, variations in R factor are not significant given the limited volume of magma in the mush zone, and so does not significantly alter the composition of the sulfide mineralization. This interpretation is similar to those made by Mao et al. (2018) based on of the morphology and crystal size distribution of olivine and sulfide blebs in these two segments, and by Wang et al. (2023) based on the similar compositions of different textural types of magnetite in Segment II-E.

In summary, two distinct sets of processes formed the different ore types throughout the Jinchuan system. In segments III and I, the lower sulfide abundances of the disseminated ores compared to the other types of ores are largely the result of greater R factors and sulfide liquid destruction/dissolution in dynamic magma flows. In contrast, the varying sulfide abundances among the different types of ores in segments II-W and II-E are mainly related to the physical percolation and migration of originally disseminated sulfide liquid droplets. Given that the portions of the conduit system in segments III and I were likely more dynamic than those in segments II-W and II-E (Fig. 13), we suggest that the relative importance of these two sets of processes to the formation of the sulfide ore types may be related to the dynamics of the mineralizing system. That is, R factor and sulfide dissolution are more important controls on sulfide distribution rather than sulfide liquid percolation in dynamic conduit systems, and vice versa.

7. Conclusions

In this contribution, we have comprehensively compared metal tenors (Cu, Ni, and the PGE) of disseminated, net-textured, massive, and Cu-rich ores from segments III, I, II-W, and II-E of the Jinchuan deposit. We modeled the behavior of Cu, PGE, and Se, during progressive enrichment processes using a multi-stage dissolution upgrading model to investigate the main processes that led to metal enrichment in each of the segments. Key conclusions from this work are provided below.

(1) The magmas from which segments III and I crystallized segregated less sulfide liquid at depth than the magmas from which segments II-W and II-E crystallized. This contributed to the generation of higher overall metal tenors in the sulfide ores in the former two segments compared to those in the latter two segments.
(2) Variations in metal tenors of disseminated ores were largely controlled by sulfide liquid–silicate melt interaction (*i.e.*, R factor), whereas those of net-textured, massive, and Cu-rich ores were largely controlled by sulfide liquid fractionation.
(3) Disseminated ores in segments III and I formed from sulfide liquids that experienced higher R factors than those that formed the other ore types. The sulfide liquids that formed the different ore types in segments II-W and II-E, however, experienced similar R factors.
(4) Massive ores have the highest IPGE, but lowest PPGE tenors among all of the ore types, which is interpreted to be the result of their formation via MSS accumulation. Copper-rich ores, however, have the lowest IPGE, but relatively high PPGE tenors, which is interpreted to be a result of their crystallization from highly fractionated sulfide liquids.
(5) Metal enrichment in each segment was governed by a multi-stage dissolution upgrading process that operated in a complex magma conduit. The portions of the conduit represented by segments III and I, however, appear to have been more dynamic, with greater influxes of magma than the portions represented by segments II-E and II-W.
(6) The ore types in segments III + I and II-W + II-E formed by different processes, with the former having formed via variable R factor in dynamic magma flows and the latter having formed by percolation of disseminated sulfide liquid.

Declaration of competing interest

The authors declare that they have no known competing financial interests or personal relationships that could have appeared to influence the work reported in this paper.

Data availability

Data will be made available on request.

Acknowledgements

This work was supported by grants from the National Natural Science Foundation of China (42272088, 41772349, 42030809), the Natural Science Foundation of Hunan Province (2023JJ40714), and the Fundamental Research Funds for the Central Universities of Central South University (506021723). We thank Zhankun Liu, Xiang Zhao, and Xiangfa Song for assistance in sample compilation. We are very grateful to three anonymous reviewers for their helpful and constructive reviews that greatly improved the quality of the final manuscript. Dr. Huayong Chen and Dr. Hongrui Fan are thanked for their efficient editorial handling of this manuscript.

Appendix A. Supplementary data

Supplementary data to this article can be found online at https://doi.org/10.1016/j.oregeorev.2023.105810.

References

Anenburg, M., Mavrogenes, J.A., 2016. Experimental observations on noble metal nanonuggets and Fe-Ti oxides, and the transport of platinum group elements in silicate melts. Geochim. Cosmchim. Acta. 192, 258–278.
Barnes, S.J., Taranovic, V., Schoneveld, L., Mansur, E., Le, Vaillant, M., Dare, S., Staude, S., Evans, N., Blanks, D., 2020. The occurrence and origin of pentlandite-chalcopyrite-pyrrhotite loop textures in magmatic Ni-Cu sulfide ores. Econ. Geol. 115, 1777-1798.
Barnes, S.J., Lightfoot, P., 2005. Formation of magmatic nickel-sulfide ore deposits and processes affecting their copper and platinum-group element contents. Econ. Geol. 100, 179–213.
Barnes, S.J., Ripley, E.M., 2016. Highly siderophile and strongly chalcophile elements in magmatic ore deposits. Rev. Mineral. Geochem. 81, 725–774.
Barnes, S.J., Mungall, J.E., Maier, W.D., 2015. Platinum group elements in mantle melts and mantle samples. Lithos 232, 395–417.
Ballhaus, C., Tredoux, M., Späth, A., 2001. Phase relations in the Fe–Ni–Cu–PGE–S system at magmatic temperature and application to massive sulphide ores of the Sudbury igneous complex. J. Petrol. 42 ((10), 1911–1926.
Barnes, S.J., Cruden, A.R., Arndt, N., Saumur, B.M., 2016. The mineral system approach applied to magmatic Ni-Cu-PGE sulphide deposits. Ore. Geol. Rev. 76, 296–316.
S.J. Barnes J.E. Mungall Le, Vaillant.M., Godel, B., Lesher, C.M., Holwell, D., Lightfoot, P. C., Krivolutskaya, N., Wei, B., Sulfide-silicate textures in magmatic Ni-Cu-PGE sulfide ore deposits: disseminated and net-textured ores Am. Mineral. 102 2017 473 506.
Barnes, S.J., Staude, S., Le, V.M., Piña, R., Lightfoot, P.C., 2018. Sulfide-silicate textures in magmatic Ni-Cu-PGE sulfide ore deposits: massive, semi-massive and sulfide-matrix breccia ores. Ore. Geol. Rev. 101, 629–651.
Barnes, S.J., Stanley, C.R., Taranovic, V., 2022. Compositions and Ni-Cu-Platinum Group Element Tenors of Nova-Bollinger Ores with Implications for the Origin of Pt Anomalies in Platinum Group Element-Poor Massive Sulfides. Econ. Geol. 117 (8), 1687–1707.
Brzozowski, M.J., Good, D., Wu, C., 2021a. Iron isotope fractionation during sulfide liquid evolution in Cu–PGE mineralization of the eastern Gabbro, Coldwell Complex, Canada. Chem. Geol. 576, 120282.
Brzozowski, M.J., Good, D.J., Wu, C., Li, W., 2021b. Cu isotope systematics of conduit-type Cu–PGE mineralization in the eastern Gabbro, Coldwell Complex, Canada. Mineral. Deposita. 56, 707–724.
Brzozowski, M., Hollings, P., Heggie, G., MacTavish, A., Wilton, D., Evans-Lamswood, D., 2023. Characterizing the supra- and subsolidus processes that generated the Current PGE–Cu–Ni deposit, Thunder Bay North Intrusive Complex, Canada: insights from trace elements and multiple S isotopes of sulfides. Published online, Mineral. Deposita.
Brzozowski, M.J., Samson, I.M., Gagnon, J.E., Good, D.J., Linnen, R.L., 2020. On the mechanisms for low-sulfide, high-platinum group element and high-sulfide, low-platinum group element mineralization in the eastern Gabbro, Coldwell Complex, Canada: evidence from textural associations, S/Se values, and platinum group element concentrations of base metal sulfides. Econ. Geol. 115, 355–384.
Campbell, I.H., Naldrett, A.J., 1979. The influence of silicate:sulfide ratios on the geochemistry of magmatic sulfides. Econ. Geol. 74, 1503–1506.
Cao, Y., Good, D., Linnen, R., Samson, I., Ruthart, R., 2021. Genesis of the low sulfide-high-grade PGE mineralization in the W Horizon, Coldwell Complex, Canada: quantitative modeling for PGE reef-style mineralization in syn-magmatic sills. Miner. Deposita. 56 (56), 1151–1176.
Chai, G., Naldrett, A.J., 1992a. The Jinchuan ultramafic intrusion: cumulate of a high-Mg basaltic magma. J. Petrol. 33, 277–303.
Chai, G., Naldrett, A.J., 1992b. Characteristics of Ni-Cu-PGE mineralization and genesis of the Jinchuan deposit, northwest China. Econ. Geol. 87, 1475–1495.
Chen, L.M., Song, X.Y., Keays, R.R., Tian, Y.L., Xiao, J.F., 2013. Segregation and fractionation of magmatic Ni-Cu-PGE sulfides in the western Jinchuan intrusion, northwestern China: insights from platinum group element geochemistry. Econ. Geol. 108, 1793–1811.
Chen, L.M., Song, X.Y., Danyushevsky, L.V., Wang, Y.S., Tian, Y.L., Xiao, J.F., 2015.A. laser ablation ICP-MS study of platinum-group and chalcophile elements in base metal sulfide minerals of the Jinchuan Ni-Cu sulfide deposit, NW China. Ore Geol. Rev. 65, 955–967.
Craig, J.R., Kullerud, G., 1969. Phase relations in the Cu-Fe-Ni-S system and their application to magmatic ore deposits. Econ. Geol. Monograph. 4, 344–358.
Dare, S.A.S., Barnes, S.J., Beaudoin, G., Méric, J., Boutroy, E., Potvin-Doucet, C., 2014. Trace elements in magnetite as petrogenetic indicators. Mineral. Deposita 49, 785–796.
Ding, X., Ripley, E., Li, C., 2012. PGE geochemistry of the Eagle Ni-Cu-(PGE) deposit, Upper Michigan: constraints on ore genesis in a dynamic magma conduit. Miner. Deposita 47, 89–104.
Duan, J., Li, C.S., Qian, Z., Jiao, J.G., Ripley, E.M., Feng, Y., 2016. Multiple S isotopes, zircon Hf isotopes, whole-rock Sr-Nd isotopes, and spatial variations of PGE tenors in the Jinchuan Ni-Cu-PGE deposit, NW China. Miner. Deposita 51, 557–574.

Duran, C.J., Barne,s S.J., Pleše, P., Kudrna, Prašek.M., Zientek, M.L., Pagé, P., 2017. Fractional crystallization-induced variations in sulfides from the Noril'sk-Talnakh mining district (polar Siberia, Russia). Ore. Geol. Rev. 90, 326-351.
Eckstrand, O.R., Hulbert, L.J., 1987. Selenium and the Source of Sulfur in Magmatic Nickel and Palladium Deposits 12, 40.
Han, Y.X., 2021. The comparative study on platinum group elements in Jinchuan and Xiarihamu magmatic Cu-Ni sulfide deposits. Chang'an University (in Chinese with English abstract). Ph.D. thesis.
Holwell, D.A., Adeyemi, Z., Ward, L.A., Smith, D.J., Graham, S.D., McDonald, I., Smith, J.W., 2017. Low temperature alteration of magmatic Ni-Cu-PGE sulfides as a source for hydrothermal Ni and PGE ores: a quantitative approach using automated mineralogy. Ore. Geol. Rev. 91, 718–740.
Jiang, J.J., Song, X.Y., Chen, L.M., Wang, L., Fu, Z.Q., 2014. Geochemistry and petrogenetic significances of semimetal and platinum group elements of the Longshou mine of Jinchuan Ni-Cu sulfide deposit. B. Mineral. Geochem. 6 (33), 882–892 in Chinese with English abstract.
Jiao, J., Rui, H., Duan, J., 2018. Genesis of the main types of sulphide ore in the Jinchuan Ni-Cu-PGE deposit, NW China: constraints from texture and mineral chemistry of pyrrhotite. Geol, J 53, 147–158.
Jiao, J.G., Tang, Z.L., Yan, H.Q., Xu, G., He, K., Duan, J., 2012. PGE characteristics of Cu-rich ores in the Jinchuan Cu-Ni sulfide deposit and its genesis. NW Geol. 45 (4), 242–1225 in Chinese with English abstract.
Kamenetsky, V., Park, J.W., Mungall, J., Pushkarev, E., Ivanov, A., Kamenetsky, M., Yaxley, G., 2015. Crystallization of platinum-group minerals from silicate melts: evidence from Cr-spinel–hosted inclusions in volcanic rocks. Geology 43, 903–906.
Kang, J., Song, X.Y., Long, T.M., Liang, Q.L., Barnes, S.J., Chen, L.M., Li, D.X., Ai, Q.X., Gao, Y.L., 2022. Lithologic and geochemical constraints on the genesis of a newly discovered orebody in the Jinchuan intrusion, NW China. Econ. Geol. 117 (8), 1809–1825.
Kerr, A., 2001. The Calculation and use of sulfide metal contents in the study of magmatic ore deposits: a methodological analysis. Explor. Min. Geol. 10, 289–301.
Kerr, A., Leitch, A.M., 2005. Self-destructive sulfide segregation systems and the formation of high-grade magmatic ore deposits. Econ. Geol. 100, 311–332.
Li, C., Barnes, S.J., Makovicky, E., Rose-Hansen, J., Makovicky, M., 1996. Partitioning of nickel, copper, iridium, rhenium, platinum, and palladium between monosulfide solid solution and sulfide liquid: effects of composition and temperature. Geochim. Cosmchim. Acta 60, 1231–1238.
Li, Y.Z., Mungall, J.E., 2022. Chalcophile element heterogeneity in Ni-Cu-(platinum group element) orebodies of Raglan Horizon in Cape Smith Belt: implications for ore-forming processes. Econ. Geol. 117 (5), 1131–1148.
Li, C., Ripley, E., 2009. Sulfur contents at sulfide-liquid or anhydrite saturation in silicate melts: empirical equations and example applications. Econ. Geol. 104, 405–412.
Li, C., Ripley, E., 2011. The Giant Jinchuan Ni-Cu-(PGE) Deposit tectonic setting, magma evolution, ore genesis, and exploration implications. Econ. Geol. 17, 163–180.
Liang, Q.L., Song, X.Y., Wirth, R., Chen, L.M., Yu, S.Y., Krivolutskaya, N.A., Dai, Z.-H., 2022. Thermodynamic conditions control the valences state of semimetals thus affecting the behavior of PGE in magmatic sulfide liquids. Geochim. Cosmochim. Acta 321, 1–15.
Lightfoot, P.C., Keays, R.R., Evans-Lamswood, D., Wheeler, R., 2012. S saturation history of Nain Plutonic Suite mafic intrusions: origin of the Voisey's Bay Ni–Cu–Co sulfide deposit, Labrador, Canada. Miner. Deposita 47, 23–50.
Liu, Y., Hu, Z., Gao, S., Günther, D., Xu, J., Gao, C., Chen, H., 2008. In situ analysis of major and trace elements of anhydrous minerals by LA-ICP-MS without applying an internal standard. Chem. Geol. 257 (1), 34–43.
Long, T.M., Song, X.Y., Kang, J., Laing, Q.L., Wang. Y.C., Li., D.X., Ai, Q.X., Suo, W.D., Lu, J.Q., 2023. Genesis of No. 2 orebody of the Jinchuan magmatic Ni-Cu-(PGE) sulfde deposit, NW China: New constraints from the newly discovered deep extension. Miner. Deposita. In press.
Maier, W., Sliep, J., Barnes, S.J., de Waal, S., Li, C., 2001. PGE-bearing mafic-ultramafic sills in the floor of the eastern Bushveld Complex on the farms Blaauwboschkraal, Zwartkopje, and Waterval. S. Afr. J. Geol. 104, 343–354.
Mansur, E.T., Barnes, S.J., Duran, C.J., 2021. An overview of chalcophile element contents of pyrrhotite, pentlandite, chalcopyrite, and pyrite from magmatic Ni-Cu-PGE sulfide deposits. Miner. Deposita 56, 179–204.
Mao, Y., Barnes, S.J., Duan, J., Qin, K.Z., Godel, B., Jiao, J., 2018. Morphology and particle size distribution of olivines and sulphides in the Jinchuan Ni–Cu sulphide deposit: evidence for sulphide percolation in a crystal mush. J. Petrol. 59 (9), 1701–1730.
Mao, X., Li, L., Liu, Z., Zeng, R., Ai, Q., 2019. Multiple magma conduits model of the Jinchuan Ni-Cu-(PGE) deposit, northwestern China: constraints from the geochemistry of platinum-group elements. Minerals 9 (3), 187.
McDonough, W.F., Sun, S., 1995. The composition of the Earth. Chem. Geol. 120, 223–253.
Mungall, J.E., Brenan, J., 2014. Partitioning of platinum-group elements and Au between sulfide liquid and basalt and the origins of mantle-crust fractionation of the chalcophile elements. Geochim. Cosmchim. Acta 125, 265–289.
Mungall, J.E., Andrews, D.R.A., Cabri, L.J., Sylvester, P.J., Tubrett, M., 2005. Partitioning of Cu, Ni, Au, and platinum-group elements between monosulfide solid solution and sulfide melt under controlled oxygen and sulfur fugacities. Geochim. Cosmchim. Acta 69, 4349–4360.
Naldrett, A.J., Craig, J.R., Kullerud, G., 1967. The central portion of the Fe-Ni-S system and its bearing on pentlandite exsolution in iron-nickel sulfide ores. Econ. Geol. 62, 826–847.
Naldrett, A.J., Wilson, A., Kinnaird, J., Chunnett, G., 2009. PGE tenor and metal ratios within and below the Merensky Reef, Bushveld Complex: implications for its genesis. J. Petrol. 50, 625–659.
Palme, H., O'Neill, H., 2014. Cosmochemical estimates of mantle composition. In: Holland HD, Turekian KK (eds) Treatise on Geochemistry (Second Edition). 3, 1-39.
Peach, C.L., Mathez, E.A., Keays, R.R., Reeves, S.J., 1994. Experimentally determined sulfide melt-silicate melt partition-coefficients for iridium and palladium. Chem. Geol. 117, 361–377.
Prichard, H.M., Knight, R.D., Fisher, P.C., McDonald, I., Zhou, M.F., 2013. Distribution of platinum-group elements in magmatic and altered ores in the Jinchuan intrusion, China: an example of selenium remobilization by postmagmatic fluids. Miner. Deposita 48, 767–786.
Qi, L., Zhou, M.F., Wang, C.Y., 2004. Determination of low concentrations of platinum group elements in geological samples by ID-ICP-MS. J. Anal. Spectrom. 19, 1335–1339.
Queffurus, M., Barnes, S.J., 2015. A review of sulfur to selenium ratios in magmatic nickel–copper and platinum-group element deposits. Ore. Geol. Rev. 69, 301–324.
Ripley, E.M., Li, C.S., 2013. Sulfide saturation in mafic magmas: is external sulfur required for magmatic Ni-Cu-(PGE) ore genesis? Econ. Geol. 108, 45–58.
Robertson, J., Ripley, E.M., Barnes, S.J., Li, C.S., 2015. Sulfur liberation from country rocks and incorporation in mafic magmas. Econ. Geol. 110, 1111–1123.
Robertson, J., Barnes, S.J., Le Vaillant, M., 2016. Dynamics of magmatic sulphide droplets during transport in silicate melts and implications for magmatic sulphide ore formation. J. Petrol. 56, 2445–2472.
Samalens, N., Barnes, S.J., Sawyer, E.W., 2017. The role of black shales as a source of sulfur and semimetals in magmatic nickel-copper deposits: example from the Partridge River Intrusion, Duluth Complex, Minnesota, USA. Ore. Geol. Rev. 81, 173–187.
Smith, J.W., Holwell, D.A., McDonald, I., Boyce, A.J., 2016. The application of S isotopes and S/Se ratios in determining ore-forming processes of magmatic Ni–Cu–PGE sulfide deposits: A cautionary case study from the northern Bushveld Complex. Ore. Geol. Rev. 73, 148–174.
Song, X.Y., Zhou, M.F., Wang, C.Y., Qi, L., Zhang, C.J., 2006. Role of crustal contamination in formation of the Jinchuan intrusion and its world-class Ni-Cu-(PGE) sulfide deposit, Northwest China. Int. Geol. Rev. 48, 1113–1132.
Song, X.Y., Keays, R.R., Zhou, M.F., Qi, L., Ihlenfeld, C., Xiao, J.F., 2009. Siderophile and chalcophile elemental constraints on the origin of the Jinchuan Ni-Cu-(PGE) sulfide deposit, NW China. Geochim. Cosmchim. Acta 73, 404–424.
Song, X.Y., Danyushevsky, L.V., Keays, R.R., Chen, L.M., Wang, Y.S., Tian, Y.L., Xiao, J. F., 2012. Structural, lithological, and geochemical constraints on the dynamic magma plumbing system of the Jinchuan Ni–Cu sulfide deposit, NW China. Miner. Deposita 47, 277–297.
Su, S.G., Li, C.S., Zhou, M.F., Ripley, E.M., Qi, L., 2008. Controls on variations of platinum-group element concentrations in the sulfide ores of the Jinchuan Ni-Cu deposit, western China. Miner. Deposita 43, 609–622.
Tang, Z.L., Li, W.Y., 1995. Mineralization model and geology of the Jinchuan deposit bearing PGE. Geological Publishing House, Beijing (in Chinese).
Tonnelier, N., 2010. Geology and genesis of the Jinchuan Ni-Cu-(PGE) deposit. Laurentian University, Sudbury, Canada, China, p. 214.
Wang, Y.H., Lai, J.Q., Cao, Y.H., Mao, X.C., Liu, X.H., Peng, L., Ai, Q.X., 2022. Partial least squares-discriminant analysis of the major and trace elements and their evolutionary characteristics from the Jinchuan Ni-Cu-(PGE) sulfide deposit, NW China. Minerals 12 (10), 1301.
Wang, Y.H., Lai, J.Q., Cao, Y.H., Brzozowski, M., 2023. Compositional variations of magnetite in different sulfide ore types in the Jinchuan Ni-Cu-PGE sulfide deposit, NW China: Insights into the mineralizing processes of conduit-type systems. Chem. Geol. 637, 121679.
Yamamoto, M., 1976. Relationship between Se/S and sulfur isotope ratios of hydrothermal sulfide minerals. Miner. Deposita 11, 197–209.
Yao, Z., Mungall, J.E., Qin, K., 2019. A preliminary model for the migration of sulfide droplets in a magmatic conduit and the significance of volatiles. J. Petrol. 60, 2281–2316.
Yao, Z., Mungall, J.E., 2022. Transport and deposition of immiscible sulfide liquid during lateral magma flow. Earth-Sci. Rev. 227, 103964.
Zhang, M., Kamo, S.L., Li, C., Hu, P., Ripley, E.M., 2010. Precise U-Pb zircon–baddeleyite age of the Jinchuan sulfide ore-bearing ultramafic intrusion, western China. Miner. Deposita 45, 3–9.